Research Square

Preprints are preliminary reports that have not undergone peer review.
They should not be considered conclusive, used to inform clinical practice,
or referenced by the media as validated information.

CPSF6 coordinates adipogenesis and metabolic homeostasis through alternative polyadenylation-mediated modulation of GSK3β

Yong Zhu
yongz59@icloud.com
Chongqing Medical University
Xianyan Zeng
Chongqing Medical University
Wenhua Xie
Chongqing Medical University
Ting Zeng
Chongqing Medical University
Yang Zhou
Chongqing Medical University
Jiyao Rao
Chongqing Medical University
Zhaoyu Zhai
Chongqing Medical University
Zheqi Lou
Chongqing Medical University
Yewei Cui
Chongqing Medical University
Peizhen Du
Chongqing Medical University
Xinyan Dai
Chongqing Medical University
Yuhang Wang
Chongqing Medical University
Jianbo Pan
Chongqing Medical University https://orcid.org/0000-0001-6014-8160
Xueya Zhao
Chongqing Medical University
Xi Xi Li

Center for Obesity and Metabolic Diseases Research, School of Basic Medicine, Chongqing Medical University https://orcid.org/0000-0002-2716-7308

Article

Keywords:

Posted Date: November 13th, 2026

DOI: https://doi.org/10.21203/rs.3.rs-11319781/v1

License: This work is licensed under a Creative Commons Attribution 4.0 International License. Read Full License

Additional Declarations: There is **NO** Competing Interest.

CPSF6 coordinates adipogenesis and metabolic homeostasis through alternative polyadenylation-mediated modulation of GSK3β

Xianyan Zeng[1, 2, 8], Wenhua Xie[2, 5, 8], Ting Zeng[2, 6, 8], Yang Zhou[3, 8], Jiyao Rao[2], Zhaoyu Zhai[4], Zheqi Lou[1, 2, 7], Yewei Cui[2], Peizhen Du[2], Xinyan Dai[2], Yuhang Wang[2], Jianbo Pan[4], Xueya Zhao[3*], Xi Li[2, 6*], Yong Zhu[1, 2, 7*]

[1] Department of Obstetrics and Gynecology, Chongqing Health Center for Women and Children, Chongqing Medical University, Chongqing 400016, China

[2] School of Basic Medical Sciences, Chongqing Medical University, Chongqing 400016, China

[3] College of Artificial Intelligence Medicine, Chongqing Medical University, Chongqing 400016, China

[4] Basic Medicine Research and Innovation Center for Novel Target and Therapeutic Intervention, Ministry of Education, College of Pharmacy, Chongqing Medical University, Chongqing 400016, China

[5] Department of Clinical Laboratory Medicine, People's Hospital of Ningxia Hui Autonomous Region, Ningxia Medical University, Ningxia Hui Autonomous Region, Yinchuan 750002, China

[6] Key Laboratory of Chromatin Homeostasis and Disease, Chongqing Education Commission of China, Chongqing Medical University, Chongqing 400016, China

[7] NHC Key Laboratory of Birth Defects and Reproductive Health, Chongqing, 401147, China

[8] These authors contributed equally to this work

[*] **Correspondence:**

yongz59@icloud.com (Y. Zhu), lixi@cqmu.edu.cn (X. Li), hutuxueya@cqmu.edu.cn (X. Zhao)

Highlights

1. APA profiling reveals obesity-associated APA remodeling and identifies CPSF6 as a regulator of adipogenesis
2. CPSF6 is required for adipocyte differentiation and white adipose tissue development
3. In mice, loss of *Cpsf6* in adipocyte precursors causes partial lipodystrophy and metabolic dysfunction
4. CPSF6-dependent *Gsk3b* 3'UTR switching activates the GSK3β–C/EBPβ axis to drive adipogenesis

Summary

Healthy expansion of white adipose tissue (WAT) depends on efficient adipogenesis to preserve systemic metabolic homeostasis, yet the molecular mechanisms of RNA 3'-end processing that govern adipogenesis remain incompletely characterized. Through integration of human obesity transcriptomes with genome-wide alternative polyadenylation (APA) profiling, we identify CPSF6 (Cleavage and polyadenylation specific factor 6) as a critical regulator of adipocyte differentiation. *In vivo* conditional deletion of *Cpsf6* in adipocyte progenitors results in WAT atrophy and impaired insulin sensitivity under physiological conditions, whereas deletion in mature adipocytes attenuates diet-induced weight gain and restricts adipose tissue expansion, revealing stage-dependent functions of CPSF6 in adipose tissue development and remodeling. Mechanistically, CPSF6 binds the *Gsk3b* 3'UTR and orchestrates APA-dependent isoform switching, thereby maintaining GSK3β protein abundance. Restoring GSK3β expression in *Cpsf6*-deficient cells partially rescues impaired adipogenesis. Furthermore, human genetic analyses support a role for CPSF6 in metabolic regulation. These findings reveal a CPSF6–G*sk3b* APA axis that coordinates adipogenesis and systemic metabolic homeostasis.

Introduction

Obesity is characterized by striking heterogeneity in metabolic outcomes: individuals with comparable adiposity can display distinct profiles of insulin sensitivity, lipid homeostasis, and inflammation[1-4]. This clinical variability indicates that obesity-related metabolic risk is governed not merely by total fat mass, but by the capacity of white adipose tissue (WAT) to undergo adaptive remodeling in the setting of chronic energy surplus[5,6]. At the tissue level, WAT expansion proceeds via two interconnected yet metabolically divergent mechanisms: hypertrophic growth, characterized by enlargement of existing mature adipocytes, and hyperplastic growth, in which adipocyte precursors differentiate into new, functionally competent adipocytes (adipogenesis). A pathological predominance of hypertrophic expansion is commonly associated with local hypoxia, low-grade chronic inflammation, and dysregulated adipokine secretion, thereby promoting systemic insulin resistance. Conversely, efficient hyperplastic expansion increases the lipid-buffering capacity of WAT, reduces ectopic lipid deposition, and helps preserve systemic metabolic homeostasis[7-10].

Accordingly, elucidating the molecular mechanisms that govern adipogenesis is fundamental to understanding adipose tissue plasticity and metabolic health in obesity.

Adipogenesis represents a highly coordinated cellular differentiation process governed by a transcriptional cascade centered on members of the CCAAT/enhancer-binding protein (C/EBP) family and peroxisome proliferator-activated receptor γ (PPARγ)[11-13]. During the early phase of adipogenesis (days 0-1), C/EBPβ is rapidly induced and acquires full transcriptional activity through phosphorylation by kinases, including GSK3β[14-16], thereby promoting the expression of PPARγ and C/EBPα, which in turn establish the transcriptional network that drives adipocyte maturation[17,18]. Although this classical transcriptional hierarchy has been extensively characterized, transcription factor cascades alone cannot fully explain the highly dynamic transcriptomic remodeling that occurs during adipogenesis. Emerging evidence indicates that post-transcriptional mechanisms, including RNA splicing, RNA modifications, mRNA stability, and translational control[19-22], also participate in cell differentiation, suggesting that adipogenesis is regulated by multilayered RNA regulatory networks. Among these mechanisms, alternative polyadenylation (APA)-mediated remodeling of mRNA 3'-ends represents a potential regulatory layer linking post-transcriptional RNA processing with adipogenic gene regulation. Notably, *GSK3B* harbors alternative polyadenylation sites within its 3' untranslated region (3'UTR)[23], raising the possibility that APA may intersect with the core adipogenic cascade.

Alternative polyadenylation is a prevalent mRNA 3'-end processing mechanism that generates transcript isoforms with distinct 3'UTRs through differential selection of polyadenylation sites (PASs). By altering the 3'UTR length, APA modulates mRNA stability, localization, translational efficiency, and interactions with microRNAs and RNA-binding proteins, thereby reshaping gene expression programs[24-27]. Increasing evidence indicates that APA is not merely a passive RNA processing event but rather a dynamic regulatory program involved in cell differentiation[28]. Given that adipogenesis is accompanied by extensive transcriptomic remodeling and precisely timed gene expression changes, dynamic APA reprogramming may provide an additional post-transcriptional layer that coordinates stage-specific adipogenic gene programs. Among the core factors governing PAS selection, CPSF6, a core component of the mammalian cleavage factor I (CFIm) complex, recognizes UGUA motifs upstream of PASs and has been established as a key determinant of 3'UTR length, conventionally promoting distal PAS usage[29,30]. However, whether APA is dynamically remodeled during adipogenesis, how CPSF6-mediated 3'UTR processing regulates the core adipogenic transcriptional network, and whether this regulation ultimately contributes to adipose tissue function and metabolic homeostasis remain poorly understood.

Given the unresolved role of APA in adipogenesis, we investigated how APA-mediated RNA processing orchestrates adipogenesis and adipose tissue homeostasis. Transcriptomic profiling of a human obesity cohort, together with adipogenesis models, revealed that CPSF6 is downregulated in adipose tissue of individuals with obesity yet markedly induced within the first day of adipogenesis,

preceding the activation of canonical adipogenic regulators such as PPARγ. Functional studies further established CPSF6 as a positive regulator of adipogenesis. Mechanistically, CPSF6 promotes adipogenesis by regulating 3'UTR processing of *Gsk3b*, thereby reshaping its post-transcriptional regulation and facilitating activation of the adipogenic transcriptional program. Integrating *in vitro* and *in vivo* functional genomic approaches, we further demonstrate that CPSF6 not only drives adipogenesis but also actively regulates metabolically favorable WAT plasticity and systemic metabolic homeostasis. Together, these findings identify a CPSF6-dependent APA regulatory axis involving GSK3β that links post-transcriptional RNA processing to the adipogenic transcriptional program and metabolically favorable adipose tissue remodeling.

Results

Obesity-associated APA remodeling nominates CPSF6 as a candidate regulator during adipogenesis

We systematically profiled APA in obesity using RNA-seq datasets of human subcutaneous white adipose tissue from metabolically healthy lean individuals and metabolically unhealthy obese individuals (Lean, n = 11; Obesity, n = 20; Fig. 1a). This analysis identified 16,783 polyadenylation sites (PASs), with 51.77% located within annotated 3'UTRs (Fig. 1b). The canonical polyadenylation signals AAUAAA and AUUAAA collectively accounted for approximately 35.29% of identified PASs (Extended Data Fig. 1a), and nucleotide profiling revealed characteristic A enrichment upstream and U-rich sequence enrichment downstream of cleavage sites (Fig. 1c), supporting the reliability of PAS annotation. Consistent with widespread APA regulation in adipose tissue, 30.64% of expressed genes and 25.79% of annotated 3'UTRs contained multiple PASs (Fig. 1d–e). Differential PAS usage analysis using the percentage of distal polyadenylation site usage index (*PDUI*) revealed extensive APA remodeling in obese adipose tissue, including significant 3'UTR lengthening in 438 genes and shortening in 527 genes (Fig. 1f). These APA-genes were associated with biological programs relevant to adipose dysfunction, including stress responses, RNA processing, cell adhesion, insulin responsiveness, ribosome biogenesis, and energy metabolism (Extended Data Fig. 1b). To identify core APA regulators[31,32] associated with obesity-related APA remodeling, we integrated independent RNA-seq and microarray datasets comparing adipose tissue from obese and lean individuals (Fig. 1a). Intersecting differentially expressed APA regulators from the two datasets identified CPSF6 and RBBP6. Among these, CPSF6 exhibited a more pronounced and consistent decrease across datasets (Fig. 1g–h), highlighting CPSF6 as a potential regulator involved in obesity-associated APA remodeling.

Given the close link between obesity-associated adipose dysfunction and impaired adipogenesis, we next examined APA dynamics using RNA-seq datasets from mouse stromal vascular fraction (SVF) cells at days 0, 1, 3, and 5 of adipocyte differentiation. Early adipogenesis was characterized by a shift toward distal PAS usage, with 398 genes showing 3'UTR lengthening and 321 genes showing 3'UTR shortening at day 1 (D1) relative to day 0 (D0) (Fig. 1i). GO enrichment analysis linked early

3'UTR lengthening to protein localization, small GTPase-mediated signaling, kinase activity regulation, and muscle cell differentiation, whereas early 3'UTR shortening was associated with amide metabolic processes, RNA metabolic regulation, RNA stability, and ribonucleoprotein complex-related terms (Extended Data Fig. 1c–d). As differentiation progressed, the APA landscape shifted toward 3'UTR shortening at days 3 (D3) and 5 (D5) (Fig. 1j; Extended Data Fig. 1e). Genes exhibiting shortening at later stages were primarily associated with ribonucleoprotein complex-related processes, cellular catabolism, and lipid-related metabolic programs, including phospholipid, glycerolipid, and fatty acid metabolism (Extended Data Fig. 1f–g). Together, these findings reveal a temporally coordinated APA program during adipogenesis, characterized by early 3'UTR lengthening followed by progressive shortening at later stages.

To determine whether CPSF6 expression paralleled these dynamic APA changes, we analyzed CPSF6 expression during adipogenesis. Adipogenic progression was confirmed by the upregulation of canonical adipogenic markers, including *Cebpb*, *Cebpa*, and *Pparg* (encoding C/EBPβ, C/EBPα, and PPARγ), at both mRNA and protein levels. CPSF6 mRNA levels showed a transient increase at D1 and declined thereafter. Immunoblot analysis of both primary SVF cells and C3H10T1/2 mesenchymal stem cells revealed a similar transient increase in CPSF6 protein at D1 after induction, followed by downregulation at later stages of adipogenesis (Fig. 1k–1l; Extended Data Fig. 1h–i). Notably, the transient peak of CPSF6 expression coincided with the early wave of 3'UTR lengthening, consistent with a potential role for CPSF6 in shaping the early APA landscape during adipogenesis.

CPSF6 acts as a positive regulator of adipocyte differentiation

To investigate whether CPSF6 regulates adipogenesis, we knocked down *Cpsf6* in primary SVF cells using lentiviral shRNA and then subjected them to adipogenic induction (Fig. 2a). RT-qPCR confirmed efficient *Cpsf6* knockdown, accompanied by decreased *Cebpb* mRNA levels. Immunoblot analysis further revealed corresponding reductions in C/EBPβ protein at D1 after induction (Fig. 2b–c), indicating that CPSF6 is required for early adipocyte differentiation. We next examined the impact of CPSF6 deficiency on terminal differentiation. Oil-Red O staining revealed markedly reduced lipid accumulation in *Cpsf6*-deficient cells (Fig. 2d). Consistently, protein expression of the master adipogenic regulators PPARγ and C/EBPα was substantially decreased. In parallel, mRNA expression of adipogenic and mature adipocyte marker genes, including *Cebpa*, *Pparg*, *Slc2a4*, *Adipoq*, and *Fabp4,* was also significantly reduced (Fig. 2e–f). These findings indicate that CPSF6 is required for adipocyte differentiation.

To determine whether this requirement is conserved across adipocyte differentiation models, we performed siRNA-mediated knockdown of *Cpsf6* in 3T3-L1 preadipocytes. Similar to primary SVF cells, *Cpsf6* knockdown significantly attenuated adipocyte differentiation. At D1, C/EBPβ was reduced at both mRNA and protein levels (Extended Data Fig. 2a–b). At D5, lipid accumulation was diminished, and the master adipogenic regulators PPARγ and C/EBPα were also downregulated at

both mRNA and protein levels. In addition, mRNA expression of mature adipocyte marker genes including *Slc2a4*, *Adipoq*, and *Fabp4*, was significantly lower (Extended Data Fig. 2c–e). These results demonstrate a conserved role for CPSF6 in adipocyte differentiation.

We next examined whether CPSF6 is sufficient to promote adipocyte differentiation. Ectopic expression of Flag-tagged *Cpsf6* in primary SVF cells enhanced both C/EBPβ protein and mRNA expression during the early phase of differentiation (Fig. 2g–h). At later stages, CPSF6-overexpressing cells exhibited increased lipid accumulation, accompanied by elevated expression of the key adipogenic transcription factors PPARγ and C/EBPα, as well as adipocyte marker genes including *Slc2a4*, *Adipoq*, and *Fabp4* (Fig. 2i–k). Collectively, these gain- and loss-of-function studies establish CPSF6 as a positive regulator of adipocyte differentiation. Moreover, the early induction of C/EBPβ suggests that CPSF6 acts upstream of the canonical C/EBPβ-PPARγ/C/EBPα transcriptional cascade to promote adipocyte differentiation.

Pdgfra-lineage _Cpsf6_ deficiency impairs white adipose tissue development and metabolic homeostasis

Having established CPSF6 as a key regulator of adipogenesis in *vitro*, we next investigated its physiological function in adipocyte progenitor-enriched lineages *in vivo*. We generated *Pdgfra*-lineage-specific *Cpsf6* conditional knockout mice by crossing $Cpsf6^{fl/fl}$ mice with *Pdgfra*-Cre transgenic mice, in which Cre activity has been demonstrated in adipocyte progenitors by lineage-tracing studies[33-35] (Fig. 3a). Homozygous mutant embryos exhibited severe growth retardation beginning at E11.5 and failed to survive beyond birth (Extended Data Fig. 3a–b), demonstrating an essential requirement for CPSF6 during embryonic development of the *Pdgfra* lineage. Due to the embryonic lethality of homozygous mutants, subsequent analyses were performed using viable heterozygous mice ($Cpsf6^{fl/+,\ Pdgfra\text{-Cre}}$ mice, hereafter referred to as $Cpsf6^{fl/+,\ APKO}$ mice), with Cre-negative littermates serving as controls.

Immunoblot analysis confirmed a marked reduction of CPSF6 protein in both inguinal white adipose tissue (IngWAT) and epididymal white adipose tissue (EpiWAT) of 8-week-old $Cpsf6^{fl/+,\ APKO}$ mice (Extended Data Fig. 3c). Under normal chow conditions, $Cpsf6^{fl/+,\ APKO}$ mice exhibited a sustained reduction in body weight relative to control littermates from 4 to 8 weeks of age (Fig. 3b; Extended Data Fig. 3d). Consistently, both IngWAT and EpiWAT depots were visibly smaller in $Cpsf6^{fl/+,\ APKO}$ mice, and their relative fat pad weights normalized to body weight were significantly reduced (Fig. 3c–d), indicating decreased adiposity. Histological analysis further revealed markedly smaller adipocytes in both depots, accompanied by a leftward shift in adipocyte size distribution (Fig. 3e–h). To determine whether impaired adipogenesis contributes to the reduction in adipose mass, we examined the expression of adipogenic genes in adipose tissues. RT-qPCR analysis showed significantly decreased expression of adipogenic regulators and mature adipocyte markers, including *Cebpa*, *Pparg*, *Slc2a4*, *Adipoq*, and *Fabp4* (Extended Data Fig. 3e), indicating impaired adipocyte maturation *in vivo*.

Given the central role of adipose tissue in systemic metabolic regulation, we next assessed glucose homeostasis in *Cpsf6*$^{fl/+,\ APKO}$ mice. Glucose tolerance tests (GTT) revealed impaired glucose clearance, with significantly elevated blood glucose levels following glucose administration (Fig. 3i). Similarly, insulin tolerance tests (ITT) demonstrated reduced insulin sensitivity, as evidenced by a blunted glucose-lowering response after insulin injection (Fig. 3j). Consistent with these metabolic defects, insulin-stimulated AKT phosphorylation at Ser473 was markedly reduced in both IngWAT and EpiWAT, whereas total AKT abundance remained unchanged (Fig. 3k), indicating impaired insulin signaling within white adipose tissue. Together, these findings demonstrate that CPSF6 is essential for white adipose tissue development and metabolic homeostasis *in vivo*.

Cpsf6 **depletion induces widespread 3'UTR shortening and reshapes APA patterns of adipogenesis-related genes**

Given that CPSF6 is a core component of the mRNA 3'-end processing machinery, we investigated whether CPSF6-dependent APA remodeling contributes to adipogenic regulation. We therefore performed parallel bulk RNA-seq and 3'-seq analyses in control and *Cpsf6*-knockdown 3T3-L1 cells during early adipocyte differentiation (D1) (Fig. 4a). Consistent with previous reports[30,36], both approaches independently revealed extensive APA remodeling upon *Cpsf6* knockdown, characterized predominantly by global 3'UTR shortening. Bulk RNA-seq-based APA inference identified 771 genes with shortened 3'UTRs and only 38 genes with lengthened 3'UTRs at D0 (Extended Data Fig. 4a), a pattern that remained evident at D1 (620 shortened versus 36 lengthened genes) (Fig. 4b). Similarly, 3'-seq analysis demonstrated a significant leftward shift in the cumulative distribution of the percentage of *PDUI*, indicating reduced distal PAS utilization and increased proximal PAS selection following *Cpsf*6 depletion (Fig. 4c; Extended Data Fig. 4b). Kolmogorov-Smirnov analysis confirmed the statistical significance of this shift. Together, these results identify *Cpsf6* as a major regulator of poly(A) site selection and 3'UTR length during adipogenesis.

Cross-platform integration identified 736 concordant APA-regulated genes at D0, enabling functional annotation of CPSF6-dependent APA programs (Extended Data Fig. 4c). Gene Ontology analysis revealed significant enrichment of biological processes associated with cell growth, cell-cycle progression, autophagy, and metabolic regulation, whereas KEGG pathway analysis highlighted multiple signaling pathways implicated in adipocyte lineage commitment and differentiation, including Wnt, insulin, PI3K-Akt, mTOR, MAPK, Ras, and cAMP signaling pathways (Extended Data Fig. 4d–e). These findings suggest that CPSF6-dependent APA remodeling influences key regulatory networks governing adipogenic competence even before differentiation is initiated. Because *Cpsf6* expression peaks during the early phase of adipogenic induction, we next focused on APA events occurring at D1. Integration of concordant and directionally consistent D1 APA events with curated adipogenesis-associated gene sets yielded 12 high-confidence candidate targets, including *Pdgfra*, *Wwtr1*, *Tbl1xr1*, *Noc3l*, *Hmga2*, *Lpl*, *Gsk3b*,

Sdf4, *Tbl1x*, *Lrp6*, *Grk5*, and *Rreb1* (Fig. 4d–e). Inspection of sequencing tracks using IGV revealed reduced read coverage across distal 3'UTR regions accompanied by increased usage of proximal PASs following *Cpsf6* depletion (Fig. 4f; Extended Data Fig. 4f). RT-qPCR validation further confirmed increased short 3'UTR isoform usage in 11 of the 12 candidate genes (Fig. 4g; Extended Data Fig. 4g), demonstrating that CPSF6-dependent APA remodeling preferentially targets a subset of adipogenesis-related regulators.

Among the validated APA targets, *Gsk3b* attracted particular attention owing to its established role in adipogenic commitment and Wnt/β-catenin signaling, one of the pathways most prominently enriched among CPSF6-regulated genes. In addition to undergoing substantial APA remodeling following *Cpsf6* depletion, *Gsk3b* occupied a central position within the interaction network of adipogenesis-related APA targets (Fig. 4h). These findings identify GSK3β as a candidate mechanistic link between CPSF6-dependent APA regulation and adipogenic signaling. We therefore examined whether CPSF6 directly regulates GSK3β expression through alternative polyadenylation of its 3'UTR.

CPSF6-mediated alternative polyadenylation of *Gsk3b* regulates its expression during adipogenesis

Integrative APA profiling identified *Gsk3b* as a candidate downstream target of CPSF6-mediated RNA processing and a potential mechanistic link to adipogenic signaling (Fig. 4). Immunoblot analysis further revealed that GSK3β protein levels increased progressively at days 0, 1, and 5 after induction during adipocyte differentiation of SVF cells (Extended Data Fig. 5a). These findings prompted us to test whether CPSF6 directly modulates poly(A) site choice within the *Gsk3b* 3'UTR. RIP-qPCR analysis revealed preferential enrichment of CPSF6 at the proximal PAS region, whereas association with the distal PAS region was substantially weaker (Fig. 5a–c). Consistent with this observation, RNA pull-down assays demonstrated stronger binding of CPSF6 to probes encompassing the proximal PAS than to those containing the distal PAS (Fig. 5d). Furthermore, PAS reporter assays showed that *Cpsf6* depletion selectively enhanced proximal PAS activity with minimal effects on distal PAS usage (Fig. 5e–f). Together, these findings indicate that CPSF6 preferentially associates with the proximal PAS region of *Gsk3b* and contributes to regulating poly(A) site choice within its 3'UTR.

We next assessed whether CPSF6-dependent regulation of *Gsk3b* APA observed in primary SVF cells also occurs in adipose tissue *in vivo*. In mice with conditional *Cpsf6* deletion in adipocyte progenitors, *Gsk3b* poly(A) site usage in IngWAT shifted from the distal to the proximal PAS (Extended Data Fig. 5b), demonstrating that CPSF6 regulates *Gsk3b* APA *in vivo*. We then examined the consequences of *Cpsf6* loss on *Gsk3b* transcript and protein expression. In SVF cells, *Cpsf6* depletion significantly increased *Gsk3b* mRNA abundance but markedly reduced GSK3β protein levels (Fig. 5g–h), with a similar reduction in GSK3β protein observed *in vivo* (Extended Data Fig. 5c). Conversely, CPSF6 overexpression decreased *Gsk3b* mRNA abundance while increasing

GSK3β protein levels (Extended Data Fig. 5d–e). Actinomycin D chase assays further showed that *Cpsf6* depletion prolonged, whereas CPSF6 overexpression shortened, the half-life of *Gsk3b* mRNA (Fig. 5i; Extended Data Fig. 5f), indicating that CPSF6-dependent APA modulates *Gsk3b* mRNA stability. Notably, despite the accumulation of more stable *Gsk3b* transcripts following *Cpsf6* depletion, GSK3β protein abundance was reduced, revealing a disconnect between mRNA stability and steady-state protein levels. We therefore examined whether CPSF6 also affects GSK3β protein stability. Cycloheximide (CHX) chase assays showed that *Cpsf6* depletion accelerated GSK3β degradation and shortened its protein half-life (Fig. 5j–k), indicating that CPSF6 is required to maintain GSK3β protein stability. Together, these findings reveal that CPSF6 regulates GSK3β expression at multiple post-transcriptional levels, exerting opposing effects on *Gsk3b* mRNA stability and GSK3β protein stability. The net effect of CPSF6 loss is therefore a reduction in GSK3β protein abundance despite increased *Gsk3b* transcript stability.

To determine whether reduced GSK3β expression functionally contributes to the adipogenic defects caused by *Cpsf6* loss, we restored GSK3β expression in *Cpsf6*-deficient SVF cells. GSK3β re-expression partially rescued the early adipogenic program, restoring the levels of phosphorylated and total C/EBPβ (Fig. 5l–m). It also markedly increased the expression of late adipogenic genes, including *Cebpa*, *Pparg*, *Slc2a4*, *Adipoq*, and *Fabp4* (Fig. 5n). These results indicate that impaired GSK3β signaling is an important contributor to the defective adipocyte differentiation induced by *Cpsf6* depletion. Unexpectedly, GSK3β overexpression also partially reversed the shift toward proximal PAS usage caused by *Cpsf6* depletion and increased *Cpsf6* mRNA abundance (Extended Data Fig. 5g–i). Although the mechanism underlying these effects remains unclear, these observations suggest a potential feedback relationship between CPSF6 and GSK3β. Together, our data support a model in which CPSF6-dependent APA of *Gsk3b* maintains adequate GSK3β protein levels, thereby sustaining the adipogenic transcriptional program and promoting adipocyte differentiation.

Adipocyte-specific loss of *Cpsf6* disrupts white adipose tissue homeostasis and insulin sensitivity through aberrant APA regulation of *Gsk3b*

Having defined the role of CPSF6 in adipocyte differentiation, we next investigated whether CPSF6 is also required for maintaining mature adipocyte function *in vivo*. To determine the physiological requirement of CPSF6 in adipocytes, we generated adipocyte-specific *Cpsf6* knockout mice (*Cpsf6*^{AKO}) by crossing *Cpsf6*$^{fl/fl}$ mice with *Adipoq*-Cre transgenic mice[33], using littermate *Cpsf6*$^{fl/fl}$ mice as controls (Fig. 6a). Efficient deletion of CPSF6 in white adipose tissue (WAT) was confirmed by immunoblotting and immunohistochemical analyses in 8-week-old *Cpsf6*^{AKO} mice (Extended Data Fig. 6a–6b). *Cpsf6*^{AKO} mice showed overall growth and body weight comparable to those of control littermates but exhibited a marked reduction in white adipose tissue mass (Fig. 6b–c). Consistently, the tissue weight-to-body weight ratios of both inguinal and epididymal WAT were significantly decreased in *Cpsf6*^{AKO} mice (Fig. 6d), indicating that adipocyte-specific loss of *Cpsf6*

impairs the maintenance of adipose tissue mass *in vivo*. Histological analysis revealed altered adipose tissue morphology in *Cpsf6*^{AKO} mice. H&E staining of both IngWAT and EpiWAT showed a shift in adipocyte size distribution toward larger adipocytes, and quantitative morphometric analysis confirmed an increase in the mean adipocyte cross-sectional area in both depots (Fig. 6e–h). Thus, reduced adipose tissue mass in *Cpsf6*^{AKO} mice was accompanied by marked remodeling of adipocyte size distribution.

We next examined whether adipose tissue remodeling in *Cpsf6*^{AKO} mice was associated with impaired mature adipocyte function. The expression of genes associated with mature adipocyte identity and function, including *Pparg*, *Slc2a4*, *Cebpa*, *Adipoq*, and *Fabp4*, was significantly reduced in IngWAT from *Cpsf6*^{AKO} mice (Fig. 6i), indicating disruption of the mature adipocyte transcriptional program. Indirect calorimetry further showed reduced oxygen consumption, carbon dioxide production, and heat production in *Cpsf6*^{AKO} mice (Extended Data Fig. 6c–e), consistent with reduced whole-body energy metabolism. Despite reduced adipose tissue mass, *Cpsf6*^{AKO} mice exhibited impaired glucose tolerance and insulin sensitivity (Fig. 6j–k). Accordingly, insulin-stimulated AKT phosphorylation was attenuated in adipose tissue from *Cpsf6*^{AKO} mice (Fig. 6l), indicating impaired adipose insulin signaling.

Given the CPSF6-dependent regulation of *Gsk3b* during adipogenesis, we next examined whether this regulatory relationship was preserved in mature adipose tissue. In IngWAT from *Cpsf6*^{AKO} mice, *Gsk3b* poly(A) site usage shifted toward the proximal PAS, and GSK3β protein abundance was reduced (Fig. 6m–n), indicating that the CPSF6-*Gsk3b* APA axis is maintained in mature adipose tissue. Together, these findings establish that CPSF6 in mature adipocytes is critical for maintaining adipose tissue function, insulin sensitivity, and metabolic homeostasis, although the contribution of this regulatory axis to the metabolic phenotype of *Cpsf6*^{AKO} mice remains to be determined.

Adipocyte-specific *Cpsf6* deletion limits adipose tissue expansion during diet-induced obesity, and human genetic analyses link *CPSF6* to metabolic traits

To assess the role of CPSF6 in mature adipocytes during high-fat diet (HFD) feeding, we generated *Cpsf6*^{AKO} mice and compared them with littermate *Cpsf6*$^{fl/fl}$ controls. *Cpsf6*^{AKO} mice exhibited significantly lower body weight than controls from week 3 of HFD feeding onward (Fig. 7a). Morphological analysis revealed reduced abdominal-subcutaneous fat accumulation, and both IngWAT and EpiWAT depots were smaller in volume, with decreased tissue weight-to-body weight ratios (Fig. 7b–d), indicating restricted adipose tissue expansion. H&E staining demonstrated that adipocytes in *Cpsf6*^{AKO} mice were smaller, with cell size distributions shifted toward smaller cells and a significant reduction in mean adipocyte area (Fig. 7e–h), consistent with impaired lipid storage capacity. Concordantly, the expression of adipogenic genes, including *Cebpa* and *Pparg*, was significantly downregulated in WAT of *Cpsf6*^{AKO} mice (Fig. 7i), further supporting disrupted adipogenesis in mature adipocytes.

To investigate the potential involvement of CPSF6 in human metabolic regulation, we performed integrative analyses combining GWAS, adipose tissue cis-eQTL, and cis-MR approaches. These analyses revealed that the CPSF6 locus harbors multiple genetic signals associated with adiposity-related traits, body fat percentage, and lipid metabolism. Several variants within this locus were also associated with CPSF6 expression in adipose tissues, suggesting a potential link between genetic variation and adipose CPSF6 regulation. Furthermore, cis-MR analyses indicated that genetically predicted higher adipose tissue CPSF6 expression was consistently associated with lower body fat percentage, with nominal associations observed for glycemic traits (Fig. 7j–m). Together, these findings provide human genetic evidence supporting a potential role for CPSF6 in adipose metabolic regulation and motivate further investigation of its functional contribution to metabolic homeostasis.

Discussion

In this study, our findings establish RNA 3'-end processing as a regulatory layer of adipocyte differentiation and define a CPSF6–GSK3β–C/EBPβ axis that couples alternative polyadenylation to the canonical adipogenic transcriptional cascade. We propose that CPSF6 may serve as a key APA regulator exerting critical checkpoint control over adipocyte differentiation: it primes the adipogenic transcriptional program prior to terminal differentiation and sustains mature adipocyte function during metabolic adaptation. These findings extend APA-mediated gene regulation to adipose homeostasis and suggest that dysregulation of RNA 3'-end regulatory networks may contribute to adipose metabolic disease.

Our findings expand the current understanding of adipogenesis beyond transcriptional regulation by revealing an early post-transcriptional mechanism that establishes adipogenic competence. Adipogenesis is essential for the development, renewal, and functional maintenance of white adipose tissue, and its disruption is closely linked to obesity, insulin resistance, and other metabolic disorders. While the C/EBPβ–PPARγ–C/EBPα transcriptional cascade has been extensively characterized[37], the post-transcriptional mechanisms that license early adipocyte differentiation remain poorly understood. Comparative transcriptomic analyses of publicly available adipose tissue datasets from obese and lean individuals highlighted CPSF6 as a potential regulator associated with adipose dysfunction. Notably, CPSF6 was rapidly induced during the early phase of adipogenesis (days 0-1), preceding the induction of canonical adipogenic regulators, including PPARγ, suggesting that CPSF6 acts as an early regulator of adipocyte differentiation rather than a consequence of terminal differentiation (Fig. 1). Consistent with this finding, both loss- and gain-of-function approaches demonstrated that CPSF6 is required for efficient activation of the C/EBPβ-PPARγ transcriptional cascade, highlighting its importance in establishing adipocyte differentiation. This temporal pattern positions CPSF6 upstream of the canonical transcriptional hierarchy, implying that APA-mediated RNA processing may serve as an "APA-mediated checkpoint" for the activation of the adipogenic program.

Mechanistically, our study reveals how APA-mediated transcript remodeling can regulate adipogenic signaling output by controlling a key kinase pathway. Building on the established function of CPSF6 as an RNA 3'-end processing factor that regulates alternative polyadenylation[38,39], our findings reveal that CPSF6-mediated transcript isoform remodeling establishes an early post-transcriptional checkpoint for adipogenic differentiation. We therefore integrated APA profiling with transcriptomic analyses and identified GSK3β — a key kinase that drives early adipocyte differentiation — as a downstream target of CPSF6 regulation. Intriguingly, although *Cpsf6* knockdown promoted proximal PAS usage in *Gsk3b* mRNA, CPSF6 occupancy at the proximal PAS region of *Gsk3b* exceeded that at the distal PAS (Fig. 5), at odds with the conventional view that CPSF6 preferentially facilitates distal PAS selection through enrichment at its conserved UGUA binding motifs[29,30]. This divergence indicates that CPSF6-dependent APA regulation is highly context-dependent, likely shaped by local RNA secondary structure, epigenetic state, and trans-acting factors.

Another intriguing finding was that, although 3'UTR shortening has traditionally been associated with increased gene expression through escape from miRNA-mediated repression[40,41], *Cpsf6* deficiency increased the abundance and stability of the short *Gsk3b* 3'UTR isoform yet paradoxically reduced GSK3β protein expression. Such mRNA-protein uncoupling cannot be readily explained by canonical feedback regulation of gene expression. A recent study demonstrated that distinct 3'UTR isoforms can also regulate translational efficiency, ribosome loading, and RNA-binding protein recruitment[42-44], highlighting regulatory functions of 3'UTR isoforms beyond the control of transcript abundance.

GSK3β has been recognized as a critical kinase required for adipogenesis through phosphorylation-dependent activation of its downstream effector C/EBPβ[16]. Consistent with this notion, restoration of GSK3β expression in *Cpsf6*-deficient SVF cells partially rescued the early adipogenic program, including the levels of phosphorylated and total C/EBPβ, and substantially restored the expression of late adipogenic genes, including *Cebpa*, *Pparg*, *Slc2a4*, *Adipoq*, and *Fabp4* (Fig. 5l–n). These findings indicate that impaired GSK3β signaling is a major contributor to the defective adipocyte differentiation caused by *Cpsf6* depletion. Notably, GSK3β overexpression also partially reversed the shift toward proximal PAS usage induced by *Cpsf6* depletion and increased *Cpsf6* mRNA abundance (Extended Data Fig. 5g–i), suggesting the possibility of a positive regulatory loop in which CPSF6 promotes *Gsk3b* expression via APA, while elevated GSK3β, in turn, supports CPSF6 expression.

Together, these findings establish the CPSF6–GSK3β–C/EBPβ axis as a direct molecular link between APA-mediated RNA processing and the canonical adipogenic transcriptional cascade and underscore the importance of this coupling in driving key regulatory nodes of the adipogenic program — namely, transcript-specific 3'UTR remodeling controls adipogenic signaling output by uncoupling mRNA abundance from protein production.

The stage-dependent consequences of CPSF6 deficiency highlight the importance of metabolic context in interpreting adipose regulatory networks. Having defined a role for CPSF6 in adipocyte differentiation, we next investigated whether CPSF6 is also required for maintaining adipose tissue homeostasis *in vivo*. CPSF6-dependent *Gsk3b* APA axis was observed in adipose tissue from both adipocyte progenitor- and mature adipocyte-specific *Cpsf6*-deficient mouse models. In both settings, *Cpsf6* loss increased proximal PAS usage in *Gsk3b* and reduced GSK3β protein abundance (Extended Data Fig. 5b; Fig. 6m–n). Despite this shared molecular signature, the phenotypic consequences of *Cpsf6* loss diverged by stage: *Pdgfra*-lineage-specific deletion of *Cpsf6* in adipocyte progenitors impaired WAT development, resulting in reduced adipose tissue mass, decreased adipocyte size, and compromised adipogenic capacity — indicating that CPSF6 is required for establishing adipogenic competence during development. In contrast, deletion of *Cpsf6* in mature adipocytes produced distinct phenotypes under diet-induced metabolic stress, characterized by reduced adipose tissue expansion, altered adipocyte size distribution, and impaired expression of mature adipocyte functional genes. These findings suggest that CPSF6-mediated APA remodeling may influence adipocyte differentiation through stage-biased repertoires of target genes and signaling pathways at different stages of adipose tissue development.

CPSF6 expression was reduced in adipose tissue from individuals with obesity (Fig. 1h), suggesting a potential link between *CPSF6* downregulation and obesity-related adipose remodeling. As our mouse studies demonstrate, the phenotypic consequences of *Cpsf6* deficiency are highly dependent on adipocyte developmental stage and metabolic context. This context dependence is important when interpreting the reduction of *CPSF6* in human adipose tissue, where bulk-tissue measurements do not resolve the cellular origin or functional consequence of this reduction. Under conditions of chronic energy surplus, impaired CPSF6-dependent APA may limit adipogenic hyperplasia and favor hypertrophic expansion — a state associated with local hypoxia, chronic inflammation, and insulin resistance[45,46]. Whether this maladaptive cascade is driven by reduced CPSF6 in human obesity remains an open question. Our human genetic analyses provide further population-level support for a potential role of CPSF6 in metabolic regulation (Fig. 7j–m). Together with our functional studies, these findings provide a mechanistic rationale for how CPSF6 dysregulation may influence susceptibility to metabolic diseases and suggest that targeting APA regulatory networks — rather than individual metabolic pathways — may offer a therapeutic strategy for obesity and other metabolic disorders.

Our studies have certain limitations. First, our analyses focused mainly on the white adipocyte lineage; whether CPSF6-mediated APA operates in brown adipose tissue or adipose-resident immune cells remains unclear, and studies across additional adipose depots will be needed to determine whether CPSF6 broadly regulates metabolic plasticity. Second, although GSK3β was validated as a key downstream effector, CPSF6 deficiency likely affects additional metabolic regulators through widespread APA remodeling. Defining the full repertoire of CPSF6-dependent APA targets and their functional coupling to metabolic pathways will be necessary to establish

CPSF6 as a key checkpoint in early adipocyte differentiation. Third, the molecular basis of the observed mRNA-protein uncoupling remains unresolved and will require ribosome profiling and/or translational analyses. Finally, whether CPSF6-dependent APA regulation is conserved in human adipose tissue has not yet been tested, and the therapeutic potential of targeting APA regulatory networks remains to be explored.

Methods

Ethical compliance

All animal experiments were performed in accordance with the guidelines for the care and use of laboratory animals at Chongqing Medical University and were approved by the Institutional Animal Care and Use Committee of Chongqing Medical University (approval number: IACUC-CQMU-2026-0164).

Material and reagents

The following antibodies were used for immunoblotting (IB), immunohistochemistry (IHC) and RNA immunoprecipitation (RIP), as indicated: anti-CPSF6 (Bethyl Laboratories, A301-356A; 1:2,000 for IB, 1:200 for IHC and and 4 μg per RIP), anti-C/EBPβ (Proteintech, 23431-1-AP; 1:1,000 for IB), anti-C/EBPa (Proteintech, 29388-1-AP; 1:1,000 for IB), anti-phospho-C/EBPβ (Thr235) (CST, 3084S; 1:1,000 for IB), anti-PPARγ (CST, 2435S; 1:1,000 for IB), anti-GSK3β (CST, 9315S; 1:2,000 for IB), anti-phospho-AKT (Ser473) (Proteintech, 28731-1-AP; 1:2,000 for IB), anti-AKT (Proteintech, 10176-2-AP; 1:2,000 for IB), anti-β-actin (Proteintech, 66009-1-Ig; 1:5,000 for IB), anti-HSP90 (CST, 4877S; 1:1,000 for IB), Goat anti-rabbit IgG-HRP (Proteintech, SA00001-2; 1:5,000 for IB), Goat anti-mouse IgG-HRP (Proteintech, SA00001-1; 1:5,000 for IB), normal rabbit IgG (Santa Cruz, sc-2027; 4 μg per RIP).

The reagents were purchased from the following companies: DMEM (high glucose) (Gibco, C11995500BT), DMEM/F12 (Gibco, 11330032), Protein A/G Magnetic Beads (Invitrogen, B23201), Pierce Streptavidin Magnetic Beads (Thermo, 88817), Rosiglitazone (Sigma-Aldrich, R2408), Recombinant human insulin (Solarbio, I8830), 3-Isobutyl-1-methylxanthine (Sigma-Aldrich, I7018), Bovine Calf Serum (Sigma-Aldrich, B7446), Fetal Bovine Serum (Biological Industries, 04-001-1A), Dexamethasone (Sigma-Aldrich, D4902), Biotin-14-CTP (Thermo, 19519016), Dispase II (Sigma-Aldrich, D4693), Collagenase Type VIII (Sigma-Aldrich, C2139), Biotin (Sigma-Aldrich, 14400), Cycloheximide (Sigma-Aldrich, C7698), Actinomycin D (Sigma-Aldrich, A1410), penicillin/streptomycin (Gibco, 15070063), Lipofectamine RNAiMAX (Thermo, 13778100), Lipofectamine 3000 (Thermo, L3000015), PolyJet In Vitro DNA Transfection Reagent (SignaGen, SL100688), PowerUp SYBR Green Master Mix (Thermo, A25742), TRIzol reagent (Invitrogen, 15596026), High-fat diet (HFD, 60% kcal fat, Research Diets, D12492).

Animals

Cpsf6$^{fl/fl}$ mice were generated by Cyagen Biosciences by inserting loxP sites into intron 3 and intron 4 of the *Cpsf6* locus. *Adipoq*-Cre and *Pdgfrα*-Cre driver lines were originally obtained from The Jackson Laboratory, and were purchased from Cyagen Biosciences and Southern Model Biotechnology, respectively. To generate adipocyte progenitor-specific *Cpsf6* knockout mice, *Cpsf6*$^{fl/fl}$ mice were crossed with *Pdgfrα*-Cre mice; the resulting offspring are hereafter referred to as *Cpsf6*^{APKO} mice. To generate mature adipocyte-specific *Cpsf6* knockout mice, *Cpsf6*$^{fl/fl}$ mice were crossed with *Adipoq*-Cre mice; the resulting offspring are hereafter referred to as *Cpsf6*^{AKO} mice. All transgenic mice were maintained on a C57BL/6J background, and Cre-negative *Cpsf6*$^{fl/fl}$ littermates were used as controls. Genotyping primers are listed in Supplementary Table S1.

All mice were housed under specific pathogen-free conditions in individually ventilated cages at 23 ± 2°C and 50%-65% humidity under a 12 h light/12 h dark cycle, with ad libitum access to food and water. Mice were housed at 3-5 animals per cage. For the HFD-induced obesity study, 8-week-old male mice were fed a high-fat diet (HFD) for 10 or 12 weeks.

Energy metabolism assessment

Whole-body energy metabolism was assessed by indirect calorimetry using a Comprehensive Laboratory Animal Monitoring System (CLAMS; Columbus Instruments, USA). Mice were individually housed in metabolic chambers, acclimated to the chambers for 24 h, and subsequently monitored continuously for 24 h with free access to food and water. Oxygen consumption (VO_2), carbon dioxide production (VCO_2), and heat production were measured using the OxyMax system according to the manufacturer's instructions. Metabolic parameters were normalized to individual body weight and analyzed.

Glucose tolerance test and insulin tolerance test

Male *Cpsf6*$^{fl/+,\ APKO}$ (or *Cpsf6*^{AKO}) mice and Cre-negative *Cpsf6*$^{fl/fl}$ littermate controls underwent glucose tolerance tests (GTTs) and insulin tolerance tests (ITTs) to evaluate systemic glucose homeostasis and insulin sensitivity.

For GTTs, mice were fasted overnight (12 h) and intraperitoneally injected with D-glucose (2 g/kg body weight). Blood glucose levels were measured from tail vein blood at 0, 30, 60, 90, and 120 min after glucose administration using a glucometer (OneTouch UltraEasy, LifeScan). For ITTs, mice were fasted for 4 h and intraperitoneally injected with human insulin (0.75 U/kg body weight). Blood glucose levels were monitored at 0, 30, 60, and 90 min after insulin injection.

Cell culture

HEK293FT cells were cultured in Dulbecco's modified Eagle's medium (DMEM) supplemented with 10% fetal bovine serum (FBS) and penicillin/streptomycin (100 U/mL penicillin and 100 μg/mL streptomycin). HEK293FT cells were used exclusively for lentiviral packaging. 3T3-L1 cells were kindly provided by Dr. M. Daniel Lane (Johns Hopkins University) and cultured in DMEM

containing 10% calf serum (CS), penicillin/streptomycin, and biotin. All cells were maintained at 37°C in a humidified incubator with 5% CO_2 unless otherwise specified.

Isolation and culture of primary stromal vascular fraction (SVF) cells

Inguinal white adipose tissue was harvested from 6- to 8-week-old mice, pooled, and minced. The minced tissues were digested in DMEM/F12 containing 0.075% collagenase type VIII and 0.6 U/mL Dispase®II at 37°C for 30-40 min. The reaction was neutralized by adding an equal volume of DMEM/F12 supplemented with 10% FBS, and the cell suspension was filtered through a 100 μm strainer. Following centrifugation, the top adipocyte layer and supernatant were discarded, and the stromal vascular fraction (SVF) pellet was collected and washed once with basal DMEM/F12. Cells were resuspended in growth medium consisting of DMEM/F12 supplemented with 10% FBS, penicillin/streptomycin, and biotin, seeded into culture dishes, and maintained at 37°C in a humidified incubator with 5% CO_2.

Adipocyte differentiation

For 3T3-L1 cells, two days post-confluence was designated as day 0 (D0). Cells were induced to differentiate in DMEM supplemented with 10% FBS, biotin, penicillin/streptomycin, 0.5 mM 3-isobutyl-1-methylxanthine, 1 μM dexamethasone, and 1 μg/mL insulin for 2 days (D0-D2). Cells were then cultured in DMEM supplemented with 10% FBS, biotin, penicillin/streptomycin, and 1 μg/mL insulin for 2 days, followed by culture in DMEM supplemented with 10% FBS, biotin, and penicillin/streptomycin until day 5 (D5). Primary SVF cells were induced to differentiate in growth medium supplemented with 0.5 mM IBMX, 1 μM dexamethasone, 5 μg/mL insulin, and 1 μM rosiglitazone for 2 days. Cells were then maintained in growth medium containing 5 μg/mL insulin and 1 μM rosiglitazone for an additional 2 days, followed by culture in growth medium until day 5 (D5). Fully differentiated adipocytes were subjected to Oil-Red O staining or harvested for subsequent molecular analyses.

Plasmid construction

siRNAs targeting *Cpsf6* were synthesized by Sangon Biotech (Shanghai, China). The targeting sequence was 5'-GTTCATTCTTTGGGAGTAA-3'. Oligonucleotides encoding shRNA against *Cpsf6* and primers for amplification of the full-length *Gsk3b* coding sequence (CDS) were synthesized by Tsingke Biotechnology (Beijing, China). All oligonucleotide sequences are listed in Supplementary Table S1. For shRNA-mediated knockdown of *Cpsf6*, annealed oligonucleotides were cloned into the pLKO.1 vector. For *Gsk3b* overexpression, the full-length *Gsk3b* CDS was amplified by PCR and subcloned into the pcDNA3.1 vector. A Flag-tagged *Cpsf6* expression plasmid in the pCDH-CMV-MCS-EF1-copGFP-T2A-Puro backbone was obtained from Wuhan GeneCreate Biological Engineering (Wuhan, China). All recombinant plasmids were verified by Sanger sequencing before use.

Transient transfection

For transient knockdown, cells were transfected with siRNAs targeting *Cpsf6* using Lipofectamine RNAiMAX at ~50% confluence. A non-targeting siRNA was used as a control. For overexpression, *Gsk3b* plasmids were transfected using Lipofectamine 3000, with empty vector as a control. At 6 h post-transfection, medium was replaced with fresh complete medium. Cells were harvested at 48 h, and mRNA levels of *Cpsf6* and *Gsk3b* were measured by RT-qPCR.

Lentiviral packaging

Lentiviral particles for *Cpsf6* knockdown (KD) or overexpression (OE) were produced in HEK293FT cells by co-transfection of the respective transfer plasmid (pLKO.1-*Cpsf6* shRNA for KD or pCDH-*Cpsf6* for OE) with the packaging plasmid psPAX2 and the envelope plasmid pMD2.G. Both psPAX2 and pMD2.G were kindly provided by the laboratory of Yongsheng Shi[47]. Transfections were performed using the PolyJet reagent according to the manufacturer's instructions. Viral supernatants were collected at 48 and 72 h post-transfection, pooled, clarified by centrifugation and filtration, and concentrated by ultracentrifugation at 20,000 × g for 2.5 h at 4°C. Viral pellets were resuspended in PBS, aliquoted, and stored at −80°C. Concentrated lentivirus was used to infect primary SVF cells.

Quantitative real-time PCR (RT-qPCR) analysis

Total RNA was extracted from cultured cells or tissues using TRIzol™ reagent. For reverse transcription, 1 μg of total RNA was reverse-transcribed into cDNA using the 5× All-In-One First-Strand cDNA Synthesis Kit (ABM, G592) according to the manufacturer's instructions. Quantitative real-time PCR was performed using PowerUp™ SYBR™ Green Master Mix on an ABI Prism 7500 Real-Time PCR System. Relative gene expression or the relative ratio of PAS usage was calculated using the $2^{-\Delta\Delta Ct}$ method. Primer sequences are listed in Supplementary Table S1.

RNA immunoprecipitation followed by RT-qPCR (RIP-qPCR)

SVF cells were collected at day 1 after adipogenic induction and washed twice with ice-cold PBS. Cell pellets were lysed on ice for 30 min in 400 μL RIP lysis buffer (20 mM HEPES, pH 7.9; 150 mM NaCl; 0.5 mM EDTA, pH 8.0; 10 mM KCl; 1.5 mM $MgCl_2$); 0.5% NP-40; 10% glycerol; 1.5 mM DTT; 1× protease inhibitor cocktail; and 40 U/mL RNase inhibitor. After centrifugation at 12,000 × g for 15 min at 4°C, the supernatant was collected. One-tenth of the lysate was retained as an input. For immunoprecipitation, Protein A/G magnetic beads were pre-washed with RIP wash buffer and then incubated with 4 μg anti-CPSF6 antibody or matched normal IgG for 4 h at 4°C with rotation. The antibody-bead complexes were mixed with the remaining lysate overnight at 4°C with rotation, followed by five washes with ice-cold RIP wash buffer. RNA was extracted from the beads and input samples using TRIzol reagent, and then reverse transcribed and quantified by RT-qPCR. Enrichment of target RNAs was calculated as the percentage of input and normalized to the IgG control.

Dual-luciferase reporter assay

Fragments containing the proximal PAS (pPAS) or distal PAS (dPAS) of the *Gsk3b* 3'UTR were amplified by PCR and cloned into the psiCHECK2 reporter vector digested with XhoI and NotI to generate the corresponding reporter constructs. These plasmids were then transfected into *Cpsf6*-knockdown SVF cells. Cells were harvested at 48 h after transfection, and luciferase activities were measured using the Dual-Luciferase Reporter Assay Kit (Promega, E1910) according to the manufacturer's instructions. Reporter activity was normalized to the internal control luciferase signal to evaluate the effect of *Cpsf6* knockdown on regulation mediated by distinct *Gsk3b* PAS-containing fragments. Primer sequences are listed in Supplementary Table S1.

RNA pull-down assay

To generate biotin-labeled RNA probes, gene-specific primers containing a T7 promoter sequence were designed and synthesized (primer sequences are listed in Supplementary Table S1) to amplify ~200-nt regions encompassing the proximal and distal polyadenylation sites (pPAS and dPAS, respectively) of the *Gsk3b* 3'UTR by PCR. The resulting PCR products were used as templates for *in vitro* transcription using the TranscriptAid T7 High Yield Transcription Kit (Thermo, K0441) in the presence of Biotin-14-CTP. The synthesized biotinylated RNA probes were purified, quantified, and stored at −80°C until use. SVF cell lysates collected on day 1 after adipogenic induction were incubated with biotinylated pPAS or dPAS RNA probes, followed by capture with streptavidin magnetic beads. Streptavidin beads incubated without RNA probes were included as a negative control for nonspecific bead-associated binding. The RNA pull-down samples were analyzed by immunoblotting to determine CPSF6 enrichment associated with the pPAS and dPAS probes, with β-Actin assessed as a nonspecific RNA-binding control. Input samples were analyzed in parallel as controls.

Immunoblotting

Cell and tissue lysates were prepared in RIPA buffer supplemented with protease inhibitors. Protein concentrations were determined using a BCA assay. Equal amounts of protein were separated by SDS-PAGE and transferred onto PVDF membranes. Membranes were blocked with 5% non-fat milk in TBST for 1 h at room temperature and incubated overnight at 4°C with primary antibodies against CPSF6, GSK3β, C/EBPβ, Phospho-C/EBPβ (Thr235), PPARγ, C/EBPα, Phospho-AKT (Ser473), AKT, β-Actin, and HSP90. Membranes were then washed and incubated with HRP-conjugated secondary antibodies for 1 h at room temperature. Protein signals were detected using an enhanced chemiluminescence reagent. HSP90 or β-Actin served as the loading control.

RNA-seq library preparation and sequencing

Total RNA was extracted from 3T3-L1 cells (with or without *Cpsf6* knockdown) at days 0 and 1 of adipogenic induction, and from mouse primary SVF cells at days 0, 1, 3, and 5 of differentiation using TRIzol reagent. RNA libraries were constructed using poly(A) mRNA enrichment followed by adapter ligation and PCR amplification, and were subsequently sequenced by Novogene using

the Illumina NovaSeq 6000 platform for 3T3-L1 samples and the Illumina NovaSeq X Plus platform for SVF samples.

RNA-seq data processing and transcriptomic analysis

Total RNA was extracted from the indicated samples, and libraries were constructed and sequenced as described above. Raw reads were trimmed with Trimmomatic (v0.36) to remove adapters and low-quality bases, then mapped to the mouse genome using HISAT2 (v2.1.0). Aligned reads were sorted with SAMtools (v1.9), and gene counts were quantified using featureCounts (Subread v1.6.3). Publicly available transcriptomic datasets were retrieved from the Gene Expression Omnibus (GEO). When raw sequencing files were available, reads were processed through the same pipeline; otherwise, normalized expression matrices were directly analyzed.

Differential expression analysis

For RNA-seq data, differential expression was assessed with DESeq2. For microarray data, we used the limma package. In both analyses, genes with an adjusted P value < 0.05 and an absolute log2 fold change (|log2FC|) > 1 were considered significantly changed.

APA analysis

APA events from RNA-seq datasets were identified based on differential usage of alternative 3'UTR (aUTR) and constitutive 3'UTR (cUTR) regions[48]. The aUTR and cUTR read coverage values were extracted, and differences between groups were assessed using the APAdiff function from the APAlyzer package. According to the APAreg output column, changes were classified as "UP" (3'UTR lengthening), "DN" (3'UTR shortening), or "NC" (no significant alteration). Fisher's exact test was performed to determine statistical significance, and events with $P < 0.1$ were considered significant. Volcano plots were generated using the ggplot2 package[49].

3'-seq library preparation and sequencing

Total RNA was extracted from differentiating cell samples using TRIzol reagent. 3'-seq libraries were constructed using the QuantSeq 3'mRNA-Seq Library Prep Kit (Lexogen, 016.24). Specifically, first-strand cDNA was synthesized from 250 ng of total RNA using oligo(dT) primers, followed by second-strand synthesis, library amplification, and barcode incorporation. Library quality was checked on an Agilent 2100 Bioanalyzer, and sequencing was performed on an Illumina HiSeq X Ten platform.

3'-seq-based APA analysis

APA analysis was adapted from the single-cell APA (scAPA) framework described by Shulman and Elkon (2019)[50], which uses a *PDUI*-based metric to quantify shifts between proximal and distal PAS usage. Here, the same conceptual approach was applied to bulk 3'-seq data to improve sensitivity and PAS quantification accuracy. Raw 3'-seq reads were processed using Fastp[51] (v0.23.2) for quality control and aligned to the mouse reference genome using STAR. Uniquely mapped reads

were retained for PAS quantification. PAS annotations were generated in R using the GenomicRanges package[52] and the mm10 reference dataset (mm10_REF.RData). Proximal and distal PAS regions were defined according to gene strand information, and PAS-centered windows (±100 bp) were used for read quantification with featureCounts. The *distal PAS usage index (PDUI)* was calculated as: $PDUI = ReadCount_{distal}/(ReadCount_{distal} + ReadCount_{proximal})$. APA events with a total of ≥10 PAS-associated reads across all compared samples were retained. Differential PAS usage was determined using Fisher's exact test followed by Benjamini – Hochberg correction. APA events with FDR < 0.05 and $|\Delta_PDUI| > 0.1$ were considered significant. Positive and negative Δ_PDUI values indicate increased distal or proximal PAS usage, corresponding to 3'UTR lengthening or shortening, respectively.

Integrative genetic analysis of adipose CPSF6

Genetic signals within the chr12q15 region surrounding CPSF6 were obtained from the GWAS Catalog, including associations with obesity-related traits, adiposity distribution, circulating lipid traits, type 2 diabetes (T2D), and metabolic syndrome. Genomic coordinates of candidate variants were standardized to the GRCh38 reference genome, and variants were functionally annotated and evaluated for overlap with CPSF6 cis-eQTL signals in adipose tissues. GTEx Adipose Subcutaneous and Adipose Visceral Omentum cis-eQTL data were used to select tissue-specific genetic instruments representing CPSF6 expression. These instruments were integrated with metabolic trait GWAS summary statistics from OpenGWAS for two-sample cis-Mendelian randomization analysis. Allele harmonization and effect estimation were performed using the TwoSampleMR framework. Because each exposure was represented by a single top cis-eQTL variant, the Wald ratio method was applied to estimate the association between genetically predicted adipose CPSF6 expression and metabolic traits.

H&E staining and immunohistochemistry (IHC)

Adipose tissue samples were collected from mice, fixed in 4% paraformaldehyde, paraffin-embedded, and sectioned at 5 μm thickness. Sections were subjected to H&E staining, and adipocyte size was quantified using AdipoCount software.

For immunohistochemistry (IHC), sections were subjected to heat-induced antigen retrieval, blocked, and incubated overnight at 4°C with anti-CPSF6 antibody (1:200), followed by incubation with an HRP-conjugated secondary antibody. Immunoreactivity was visualized using a DAB chromogenic substrate and counterstained with hematoxylin. Images were captured using an Olympus imaging system.

Quantification and statistical analysis

Data are presented as the mean ± SEM. Statistical analyses were performed using GraphPad Prism 8.0. Statistical significance was determined using unpaired two-tailed Student's *t* test, one-way ANOVA, or two-way ANOVA with Sidak's multiple-comparison test, as appropriate. The statistical

tests used and sample sizes are indicated in the figure legends. Statistical significance is represented as follows: $^{*}P < 0.05$, $^{**}P < 0.01$, $^{***}P < 0.001$, $^{****}P < 0.0001$.

Acknowledgments

We thank Yongsheng Shi (University of California, Irvine, CA, USA) for providing plasmids and M. Daniel Lane (Johns Hopkins University, Baltimore, MD, USA) for providing 3T3-L1 cells.

Author contributions

Conceptualization, X.-Y. Zeng, W.-H. Xie, X. Li, and Y. Zhu; investigation, X.-Y. Zeng, W.-H. Xie, J.-Y. Rao, T. Zeng, X. Li, and Y. Zhu; formal analysis, X.-Y. Zeng, T. Zeng, Y. Zhu, and X. Li; bioinformatics analysis, Z.-Y. Zhai, J.-B. Pan, Y. Zhou, and X.-Y. Zhao; writing – original draft, X.-Y. Zeng; writing – review and editing, Z.-Q. Lou, Y.-W. Cui, P.-Z. Du, X.-Y. Dai, Y.-H. Wang, and all other authors; supervision, X.-Y. Zhao, Y. Zhu, and X. Li; project administration, X.-Y. Zeng, X. Li, and Y. Zhu. All authors read and approved the final manuscript.

Data availability

The publicly available transcriptomic datasets analyzed in this study were obtained from the NCBI Sequence Read Archive (SRA) under accession numbers PRJNA641129 and PRJNA670900 (RNA-seq), and from the NCBI Gene Expression Omnibus (GEO) under accession numbers GSE55200 and GSE77962 (microarray). Newly generated RNA-seq and 3'-seq datasets from 3T3-L1 cells, along with RNA-seq datasets from SVF samples, have been deposited in the NCBI SRA under accession number PRJNA1497577. Any additional information required to reanalyze the data reported in this paper is available from the lead contact upon reasonable request.

Funding

This work was supported by grants from the National Natural Science Foundation of China (Grant No. 82070111), the Research Start-up Fund for Overseas Recruited Talents of Chongqing Medical University (Grant No. R2004), and the China Postdoctoral Science Foundation (Grant No. 2025M771947).

References

1 Yaghootkar, H. When more is not worse: Genetic subtypes of obesity challenge conventional risk paradigms. *Cell Metab* **37**, 2099-2101 (2025).

2 Schulze, M. B. & Stefan, N. Metabolically healthy obesity: from epidemiology and mechanisms to clinical implications. *Nat Rev Endocrinol* **20**, 633-646 (2024).

3 Chakaroun, R. M. *et al.* Multi-omic definition of metabolic obesity through adipose tissue-microbiome interactions. *Nat Med* **32**, 113-125 (2026).

4 Blüher, M. Metabolically Healthy Obesity. *Endocr Rev* **41** (2020).

5 Lecoutre, S. *et al.* Enhancing adipose tissue plasticity: progenitor cell roles in metabolic health. *Nat Rev Endocrinol* **21**, 272-288 (2025).

6 Rydén, M. Perspectives on human adipose tissue: from cellular mechanisms to clinical complications. *Diabetologia* **69**, 1731-1740 (2026).

7 Ghaben, A. L. & Scherer, P. E. Adipogenesis and metabolic health. *Nat Rev Mol Cell Biol* **20**, 242-258 (2019).

8 Vishvanath, L. & Gupta, R. K. Contribution of adipogenesis to healthy adipose tissue expansion in obesity. *J Clin Invest* **129**, 4022-4031 (2019).

9 Yang, Z. H. *et al.* Therapeutic targeting of white adipose tissue metabolic dysfunction in obesity: mechanisms and opportunities. *MedComm (2020)* **5**, e560 (2024).

10 Sakers, A., De Siqueira, M. K., Seale, P. & Villanueva, C. J. Adipose-tissue plasticity in health and disease. *Cell* **185**, 419-446 (2022).

11 Rocha, S., Proença, C., Carvalho, F. & Fernandes, E. Adipose Tissue Plasticity and Adipogenesis: From Cellular Mechanisms to Therapeutic Targets in Obesity. *Curr Obes Rep* **15** (2026).

12 Lane, M. D., Tang, Q. Q. & Jiang, M. S. Role of the CCAAT enhancer binding proteins (C/EBPs) in adipocyte differentiation. *Biochem Biophys Res Commun* **266**, 677-683 (1999).

13 Rosen, E. D. & MacDougald, O. A. Adipocyte differentiation from the inside out. *Nat Rev Mol Cell Biol* **7**, 885-896 (2006).

14 Tang, Q. Q., Otto, T. C. & Lane, M. D. CCAAT/enhancer-binding protein beta is required for mitotic clonal expansion during adipogenesis. *Proc Natl Acad Sci U S A* **100**, 850-855 (2003).

15 Li, X. *et al.* Role of cdk2 in the sequential phosphorylation/activation of C/EBPbeta during adipocyte differentiation. *Proc Natl Acad Sci U S A* **104**, 11597-11602 (2007).

16 Tang, Q. Q. *et al.* Sequential phosphorylation of CCAAT enhancer-binding protein beta by MAPK and glycogen synthase kinase 3beta is required for adipogenesis. *Proc Natl Acad Sci U S A* **102**, 9766-9771 (2005).

17 Sarjeant, K. & Stephens, J. M. Adipogenesis. *Cold Spring Harb Perspect Biol* **4**, a008417 (2012).

18 Lee, J. E. & Ge, K. Transcriptional and epigenetic regulation of PPARγ expression during adipogenesis. *Cell Biosci* **4**, 29 (2014).

19 Yang, Z. *et al.* NOVA1 prevents overactivation of the unfolded protein response and facilitates chromatin access during human white adipogenesis. *Nucleic Acids Res* **51**, 6981-6998 (2023).

20 Wan, X. *et al.* NAT10-mediated N4-acetylcytidine modification in KLF9 mRNA promotes adipogenesis. *Cell Death Differ* **32**, 1613-1629 (2025).

21 Wei, W. *et al.* TRIM24 is an insulin-responsive regulator of P-bodies. *Nat Commun* **13**, 3972 (2022).
22 Dumesic, P. A. *et al.* RBM43 controls PGC1α translation and a PGC1α-STING signaling axis. *Cell Metab* **37**, 742-757.e748 (2025).
23 Yu, S. *et al.* PolyA_DB v4: systematic polyA site identification and isoform annotation in human and mouse genomes using 3'end and long-read sequencing data. *Nucleic Acids Res* **54**, D247-d254 (2026).
24 Garneau, N. L., Wilusz, J. & Wilusz, C. J. The highways and byways of mRNA decay. *Nat Rev Mol Cell Biol* **8**, 113-126 (2007).
25 Chen, S. *et al.* The mRNA Export Receptor NXF1 Coordinates Transcriptional Dynamics, Alternative Polyadenylation, and mRNA Export. *Mol Cell* **74**, 118-131.e117 (2019).
26 Ruepp, M. D. *et al.* Mammalian pre-mRNA 3'end processing factor CF I m 68 functions in mRNA export. *Mol Biol Cell* **20**, 5211-5223 (2009).
27 Malka, Y. *et al.* Alternative cleavage and polyadenylation generates downstream uncapped RNA isoforms with translation potential. *Mol Cell* **82**, 3840-3855.e3848 (2022).
28 Tian, B., Yu, S. & Zhang, Q. Regulation of gene expression by alternative polyadenylation in health and disease. *Nat Rev Genet* **27**, 385-404 (2026).
29 Gruber, A. R., Martin, G., Keller, W. & Zavolan, M. Cleavage factor Im is a key regulator of 3' UTR length. *RNA Biol* **9**, 1405-1412 (2012).
30 Zhu, Y. *et al.* Molecular Mechanisms for CFIm-Mediated Regulation of mRNA Alternative Polyadenylation. *Mol Cell* **69**, 62-74.e64 (2018).
31 Shi, Y. *et al.* Molecular architecture of the human pre-mRNA 3' processing complex. *Mol Cell* **33**, 365-376 (2009).
32 Gruber, A. J. & Zavolan, M. Alternative cleavage and polyadenylation in health and disease. *Nat Rev Genet* **20**, 599-614 (2019).
33 Jeffery, E. *et al.* Characterization of Cre recombinase models for the study of adipose tissue. *Adipocyte* **3**, 206-211 (2014).
34 Zhao, G. N. *et al.* TMBIM1 is an inhibitor of adipogenesis and its depletion promotes adipocyte hyperplasia and improves obesity-related metabolic disease. *Cell Metab* **33**, 1640-1654.e1648 (2021).
35 Gao, Z. *et al.* Age-associated telomere attrition in adipocyte progenitors predisposes to metabolic disease. *Nat Metab* **2**, 1482-1497 (2020).
36 de Prisco, N. *et al.* Alternative polyadenylation alters protein dosage by switching between intronic and 3'UTR sites. *Sci Adv* **9**, eade4814 (2023).
37 Farmer, S. R. Transcriptional control of adipocyte formation. *Cell Metab* **4**, 263-273 (2006).
38 Martin, G., Gruber, A. R., Keller, W. & Zavolan, M. Genome-wide analysis of pre-mRNA 3' end processing reveals a decisive role of human cleavage factor I in the regulation of 3' UTR length. *Cell Rep* **1**, 753-763 (2012).

39 Tian, B. & Manley, J. L. Alternative polyadenylation of mRNA precursors. *Nat Rev Mol Cell Biol* **18**, 18-30 (2017).

40 Mayr, C. & Bartel, D. P. Widespread shortening of 3'UTRs by alternative cleavage and polyadenylation activates oncogenes in cancer cells. *Cell* **138**, 673-684 (2009).

41 Sandberg, R., Neilson, J. R., Sarma, A., Sharp, P. A. & Burge, C. B. Proliferating cells express mRNAs with shortened 3' untranslated regions and fewer microRNA target sites. *Science* **320**, 1643-1647 (2008).

42 West, J. D. *et al.* The quantitative impact of 3'UTRs on gene expression. *Nucleic Acids Res* **53** (2025).

43 Findlay, S. D., Romo, L. & Burge, C. B. Quantifying negative selection in human 3' UTRs uncovers constrained targets of RNA-binding proteins. *Nat Commun* **15**, 85 (2024).

44 Luo, Y., Zhong, Y., Basu, S., Wu, M. C. & Mayr, C. mRNA 3'UTRs chaperone intrinsically disordered regions to control protein activity. *Cell* **189**, 4619-4636.e4616 (2026).

45 Scherer, P. E. Adipose tissue: from lipid storage compartment to endocrine organ. *Diabetes* **55**, 1537-1545 (2006).

46 Virtue, S. & Vidal-Puig, A. Adipose tissue expandability, lipotoxicity and the Metabolic Syndrome--an allostatic perspective. *Biochim Biophys Acta* **1801**, 338-349 (2010).

47 Soles, L. V. *et al.* A nuclear RNA degradation code is recognized by PAXT for eukaryotic transcriptome surveillance. *Mol Cell* **85**, 1575-1588.e1579 (2025).

48 Wang, R. & Tian, B. APAlyzer: a bioinformatics package for analysis of alternative polyadenylation isoforms. *Bioinformatics* **36**, 3907-3909 (2020).

49 Wickham, H. *ggplot2: Elegant Graphics for Data Analysis*. 2nd edn, (Springer-Verlag, 2016).

50 Shulman, E. D. & Elkon, R. Cell-type-specific analysis of alternative polyadenylation using single-cell transcriptomics data. *Nucleic Acids Res* **47**, 10027-10039 (2019).

51 Chen, S., Zhou, Y., Chen, Y. & Gu, J. fastp: an ultra-fast all-in-one FASTQ preprocessor. *Bioinformatics* **34**, i884-i890 (2018).

52 Lawrence, M. *et al.* Software for computing and annotating genomic ranges. *PLoS Comput Biol* **9**, e1003118 (2013).

Figures

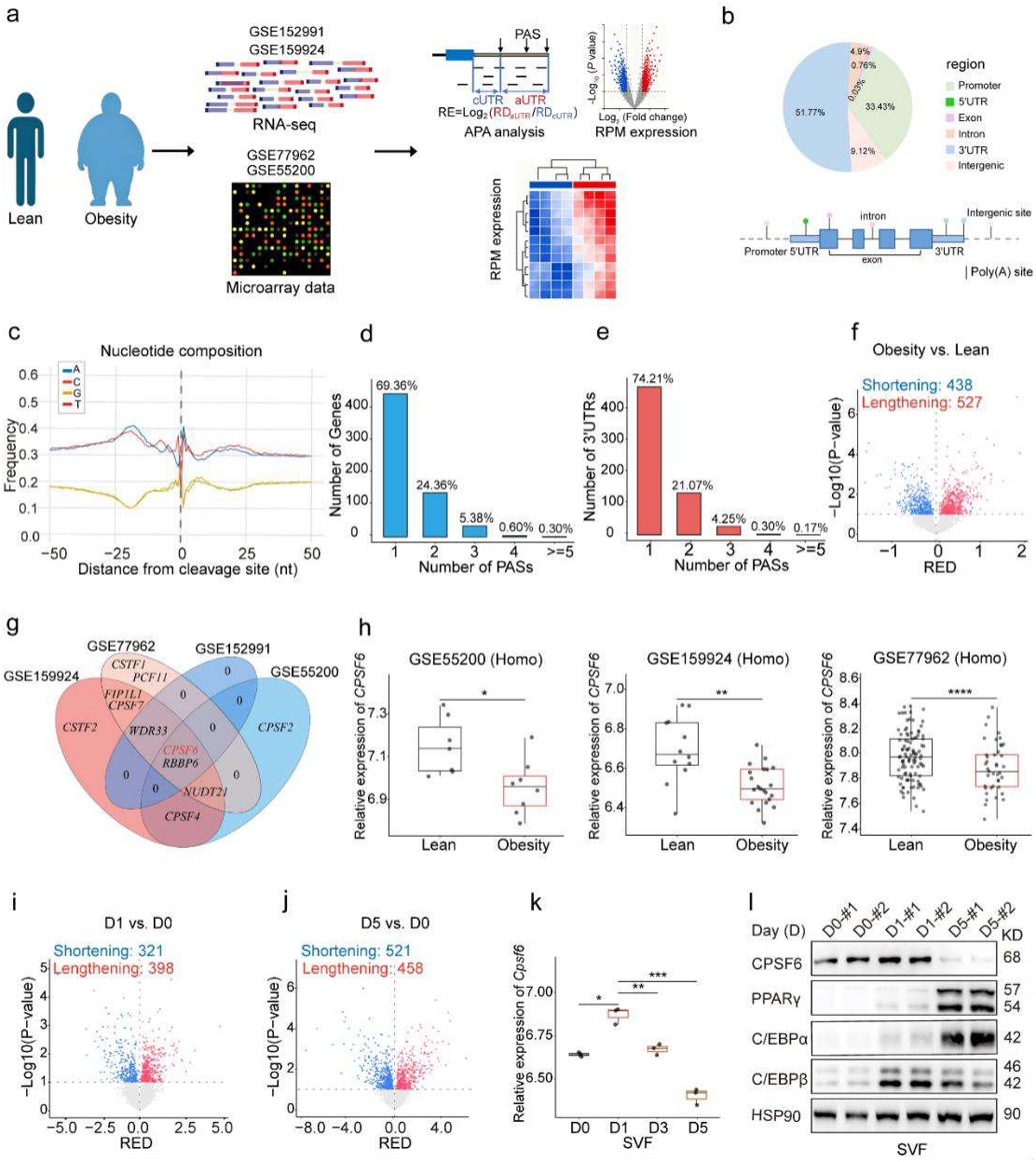


Fig. 1. Transcriptome-wide APA remodeling nominates CPSF6 as a candidate APA regulator in obesity and adipogenesis.

(a) Schematic of the integrative analysis used to characterize obesity-associated APA remodeling in human subcutaneous white adipose tissue (SAT) and identify candidate APA regulators. RNA-seq data from lean and obese human individuals (GSE152991) were analyzed to identify widespread alternative polyadenylation (APA) events in 3'UTRs. Differential APA events were defined based on a relative expression (RE) score, calculated as $\log_2(RD_{aUTR}/RD_{cUTR})$, where RD is defined as read density; aUTR and cUTR refer to the alternative and constitutive 3'UTRs, respectively. Expression changes of core APA regulators were assessed within GSE152991 and cross-validated using an independent RNA-seq dataset (GSE159924), as well as two independent microarray datasets (GSE77962 and GSE55200). **(b)** The pie chart shows the proportions of identified polyadenylation sites (PASs) across genomic

features, whereas the schematic illustrates the corresponding locations of these features within gene architecture. **(c)** Nucleotide composition within 50 nt upstream and downstream of cleavage sites. **(d-e)** Bar graphs displaying the distribution of the number of polyadenylation sites (PASs) per gene **(d)** and per 3'UTR **(e)**. Percentages denote the relative proportion of genes or 3'UTRs containing the indicated number of PASs. **(f)** Volcano plot depicting global 3'UTR length changes in human SAT from obese versus (vs.) lean individuals. The x-axis displays the relative expression difference (RED) in distal vs. proximal poly(A) site (PAS) usage; negative and positive values correspond to 3'UTR shortening and lengthening, respectively. The y-axis shows statistical significance (−log10(P-value)), with the dashed line marking the significance threshold. Significantly altered APA events are highlighted, with blue dots indicating shortening and red dots indicating lengthening. **(g)** Venn diagram illustrating the overlapping core APA regulators across four independent human GEO datasets (GSE159924, GSE55200, GSE152991, and GSE77962). The overlapping genes are listed, with *CPSF6* highlighted in red identified as a core candidate gene. **(h)** Box plots showing the relative expression levels of *CPSF6* in lean vs. obese individuals across three independent human cohorts. Each dot represents an individual subject. **(i-j)** Volcano plots illustrating global APA dynamics during adipocyte differentiation of stromal vascular fraction (SVF) cells at D1 vs. D0 **(i)** and D5 vs. D0 **(j)**. Blue and red dots denote statistically significant 3'UTR shortening (negative RED values) and lengthening (positive RED values) events, respectively. The numbers of significantly altered shortening and lengthening events are indicated in the plots. **(k)** Box plot showing relative *Cpsf6* expression in RNA-seq data during a 5-day time course of adipocyte differentiation in SVF cells. **(l)** Immunoblot analysis of CPSF6 and adipogenic markers (PPARγ, C/EBPα, and C/EBPβ) during adipocyte differentiation of SVF cells at D0, D1, and D5. HSP90 was used as an internal loading control. Molecular weights (kDa) are indicated on the right. Data are presented as mean ± SEM; $n = 3$. Statistical significance was determined by unpaired two-tailed Student's t test for two-group comparisons, or by two-way ANOVA followed by Sidak's multiple-comparison test. $^{*}P < 0.05$, $^{**}P < 0.01$, $^{***}P < 0.001$, $^{****}P < 0.0001$.

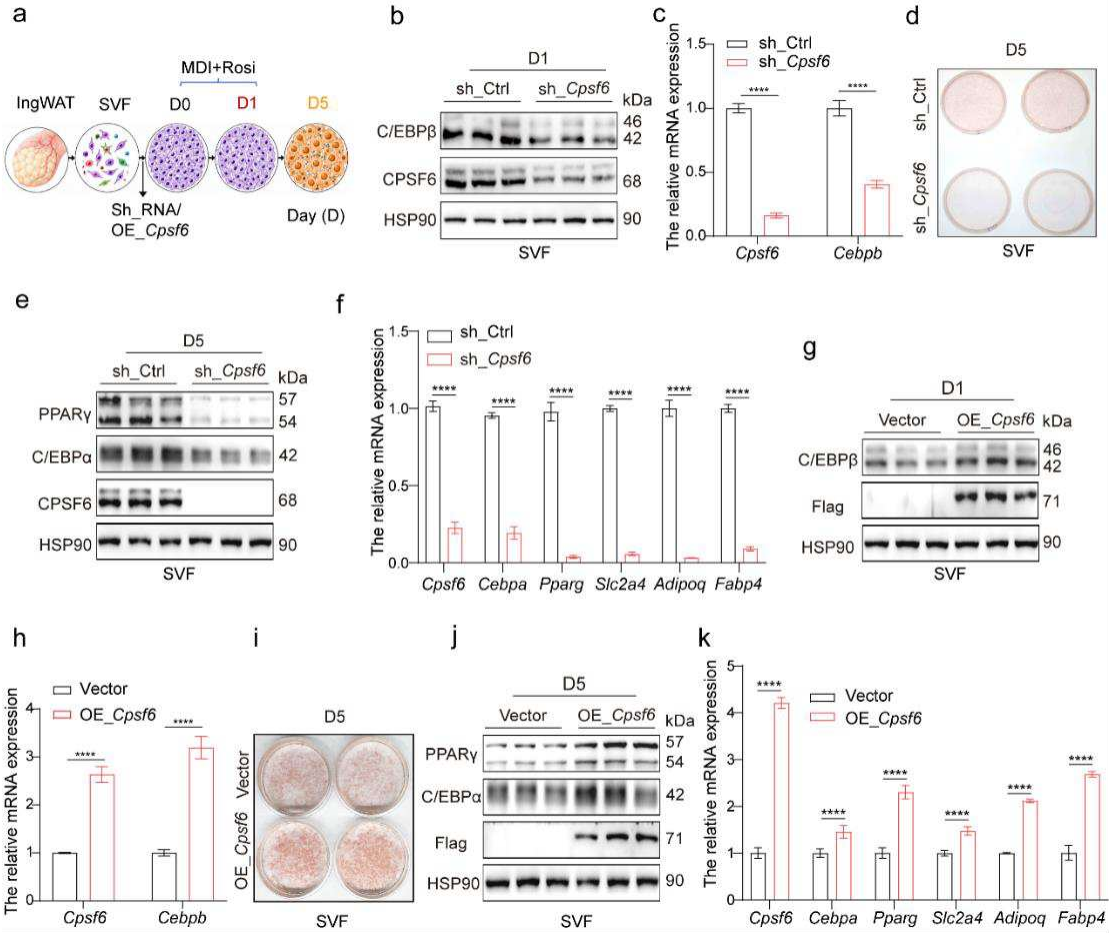


Fig. 2. CPSF6 is required for and promotes adipocyte differentiation of SVF cells in *vitro*. **(a)** Schematic of the experimental design. SVF cells isolated from mouse inguinal white adipose tissue (IngWAT) were transduced with lentiviruses encoding a *Cpsf6*-targeting short hairpin RNA (shRNA), a Flag-*Cpsf6* overexpression construct, or the corresponding control vectors before induction of adipocyte differentiation (D0). Cells were harvested at D1 and D5 of differentiation for the indicated analyses. **(b-c)** Immunoblot analysis of C/EBPβ and CPSF6 protein abundance **(b)** and RT-qPCR analysis of *Cebpb* and *Cpsf6* mRNA expression **(c)** in control and *Cpsf6*-knockdown SVF cells at D1 of adipocyte differentiation. **(d)** Representative images of Oil-Red O staining in control and *Cpsf6*-knockdown SVF cells at D5 of adipocyte differentiation. **(e-f)** Immunoblot analysis of PPARγ, C/EBPα, and CPSF6 protein levels **(e)** and RT-qPCR analysis of *Cpsf6* knockdown efficiency and adipogenic/mature adipocyte marker gene expression (*Cebpa*, *Pparg*, *Slc2a4*, *Adipoq*, and *Fabp4*) **(f)** in control and *Cpsf6*-knockdown SVF cells at D5. **(g-h)** Immunoblot analysis of C/EBPβ and Flag-CPSF6 protein abundance **(g)** and RT-qPCR analysis of total *Cpsf6* and *Cebpb* mRNA expression **(h)** in vector control and Flag-*Cpsf6*-overexpressing SVF cells at D1 of adipocyte differentiation. **(i)** Representative Oil-Red O staining of vector control and Flag-*Cpsf6*-overexpressing SVF cells at D5. **(j-k)** Immunoblot analysis of PPARγ, C/EBPα, and Flag-CPSF6 **(j)** and RT-qPCR analysis of *Cpsf6* knockdown efficiency and adipogenic/mature adipocyte marker gene expression **(k)** in control and Flag-*Cpsf6*-overexpressing SVF cells at D5 of adipocyte differentiation. Data are presented as mean ± SEM; $n = 3$. Two-way ANOVA with Sidak's multiple-comparisons test. $^{****}P < 0.0001$.

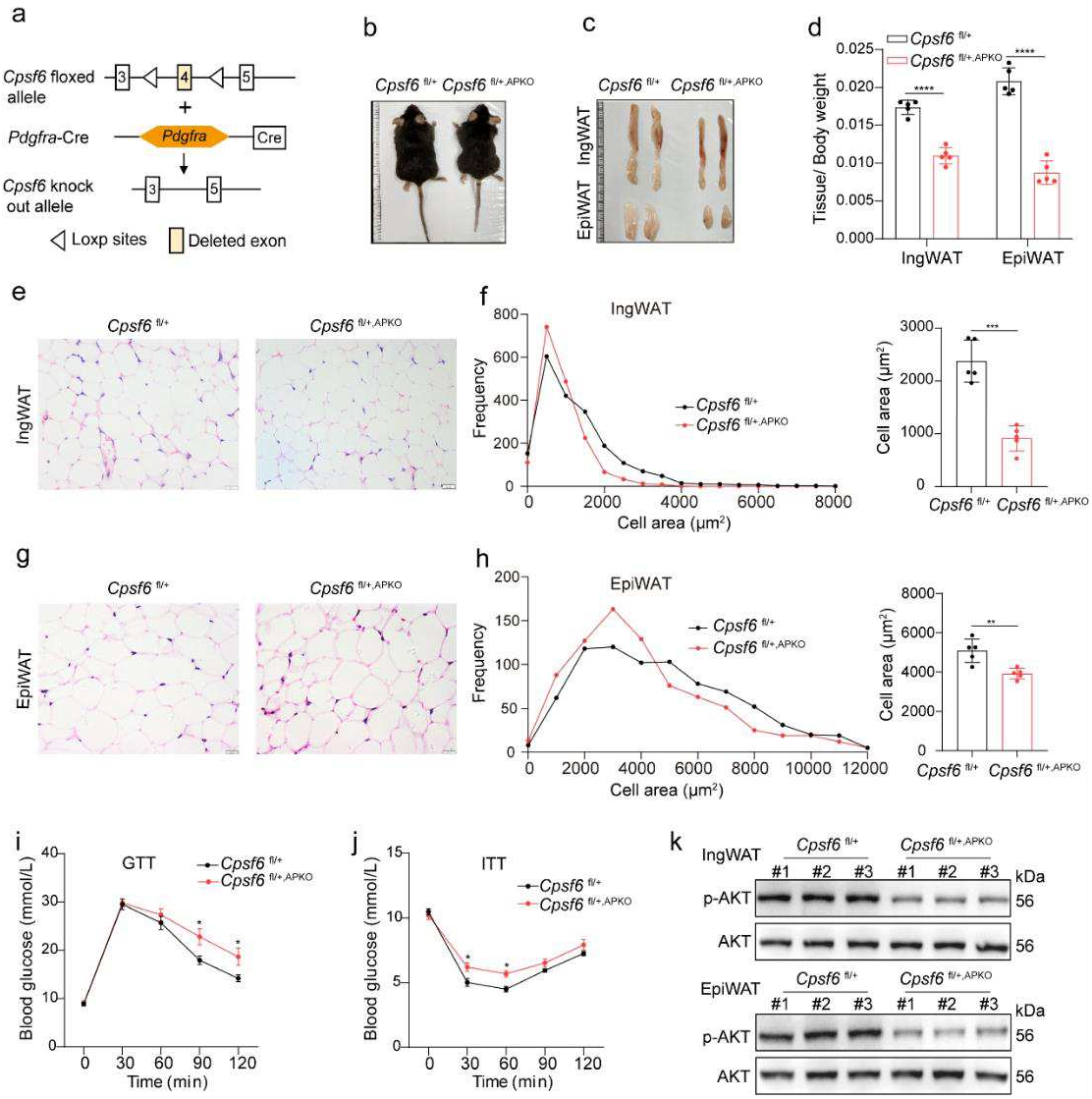


Fig. 3. *Pdgfra*-Cre–mediated *Cpsf6* deletion impairs white adipose tissue development and glucose homeostasis.

(a) Schematic of the genetic strategy. *Cpsf6*$^{fl/+,\ Pdgfra\text{-}Cre}$ mice (*Cpsf6*$^{fl/+,\ APKO}$) were generated to conditionally delete one *Cpsf6* allele in *Pdgfra*-expressing adipose progenitor cells. Male *Cpsf6*$^{fl/+,\ APKO}$ mice and *Cpsf6*$^{fl/+}$ littermate controls were analyzed at 8 weeks of age. **(b)** Representative photograph of 8-week-old *Cpsf6*$^{fl/+}$ control and *Cpsf6*$^{fl/+,\ APKO}$ mice. **(c)** Representative images of inguinal white adipose tissue (IngWAT) and epididymal white adipose tissue (EpiWAT) isolated from 8-week-old *Cpsf6*$^{fl/+}$ control and *Cpsf6*$^{fl/+,\ APKO}$ mice. **(d)** Quantification of IngWAT and EpiWAT weight normalized to body weight. ($n = 5$). **(e-h)** H&E staining and adipocyte morphometry of IngWAT **(e-f)** and EpiWAT **(g-h)**. Panels **e** and **g** show representative images, while **f** and **h** quantify adipocyte size distribution (left) and mean cross-sectional area (right) for the indicated genotypes (*Cpsf6*$^{fl/+}$ control and *Cpsf6*$^{fl/+,\ APKO}$ mice). (Scale bar = 20 μm; $n = 5$). **(i)** Glucose tolerance test (GTT) in *Cpsf6*$^{fl/+}$ and *Cpsf6*$^{fl/+,\ APKO}$ mice. Blood glucose levels were measured at the indicated time points after intraperitoneal glucose injection. ($n = 5$). **(j)** Insulin tolerance test (ITT) in *Cpsf6*$^{fl/+}$ and *Cpsf6*$^{fl/+,\ APKO}$ mice. Blood glucose concentrations were monitored after intraperitoneal insulin injection. ($n = 5$). **(k)** Immunoblot analysis of insulin-stimulated AKT phosphorylation at Ser473 in IngWAT and EpiWAT from *Cpsf6*$^{fl/+}$ and *Cpsf6*$^{fl/+,\ APKO}$ mice. Phospho-AKT was normalized to total AKT.

Data are presented as mean ± SEM. Statistical significance was determined by two-tailed unpaired Student's *t*-test or two-way ANOVA with Sidak's multiple-comparisons test. *n* values are indicated in the corresponding panels. $^{*}P < 0.05$, $^{**}P < 0.01$, $^{***}P < 0.001$, $^{****}P < 0.0001$.

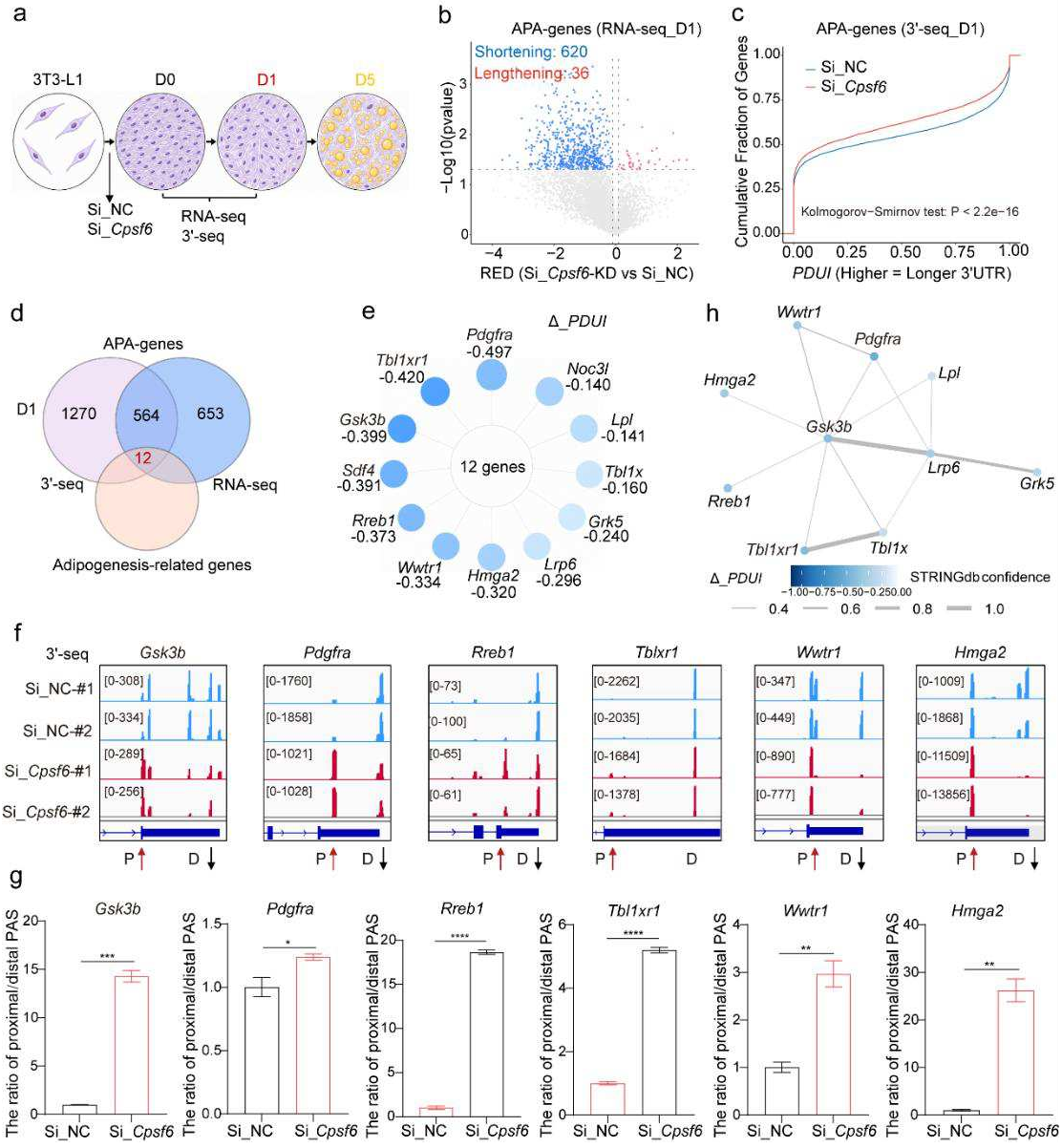


Fig. 4. CPSF6 depletion remodels the APA landscape and promotes 3'UTR shortening in adipogenesis-related genes.

(a) Schematic of the experimental workflow. 3T3-L1 preadipocytes were transfected with *Cpsf6*-targeting siRNA (si_*Cpsf6*) or non-targeting control siRNA before induction of adipocyte differentiation at D0. Cells were collected at D0 and D1 for bulk RNA-seq and 3'-seq analyses. **(b)** Volcano plot of differential APA events identified using APAlyzer from bulk RNA-seq data in control and si_*Cpsf6* cells at D1. Significantly shortened and lengthened 3'UTR events are highlighted in blue and red, respectively. The numbers of significant shortening and lengthening events are indicated. **(c)** Cumulative distribution of the percentage of distal poly(A) site usage index (*PDUI*) in control and si_*Cpsf6* cells at D1, determined by 3'-seq. Statistical significance was assessed by the Kolmogorov-Smirnov test (all $P < 2.2 \times 10^{-16}$). **(d)** Venn diagram depicting the overlap of D1 APA genes identified by 3'-seq and bulk RNA-seq with known adipogenesis-related genes. The 12 overlapping genes represent high-confidence candidates for CPSF6-dependent post-transcriptional regulation. (Supplementary Table S2). **(e)** Radial plot ranking the 12 adipogenesis-related APA genes identified from the intersection analysis in **(d).** The circle size represents the magnitude of Δ_*PDUI* (a negative

value indicates 3'UTR shortening). **(f)** Representative genome browser tracks of 3'-seq read coverage for the top six adipogenesis-related APA genes (ranked by Δ_*PDUI*) in control and si_*Cpsf6* cells at D1. Red and black arrows indicate proximal (P) and distal (D) poly(A) sites, respectively. **(g)** RT-qPCR validation of APA-associated isoform changes in representative genes shown in **(f)**, using primer sets targeting the proximal and distal regions of the 3'UTR. Primer sequences are provided in Supplementary Table S1. Data are normalized to the control group. **(h)** STRING network of 10 candidate adipogenesis-related APA genes. Of the 12 candidates identified in **(e)**, two were excluded because they were not recognized by STRING or lacked network interactions. Node color indicates Δ_*PDUI* upon *Cpsf6* knockdown; negative values denote reduced distal PAS usage (3'UTR shortening). Edge width reflects the normalized STRING combined interaction score. Data are presented as mean ± SEM; $n = 3$. Statistical significance was determined by a two-tailed unpaired Student's t-test. $^{*}P < 0.05$, $^{**}P < 0.01$, $^{***}P < 0.001$, $^{****}P < 0.0001$.

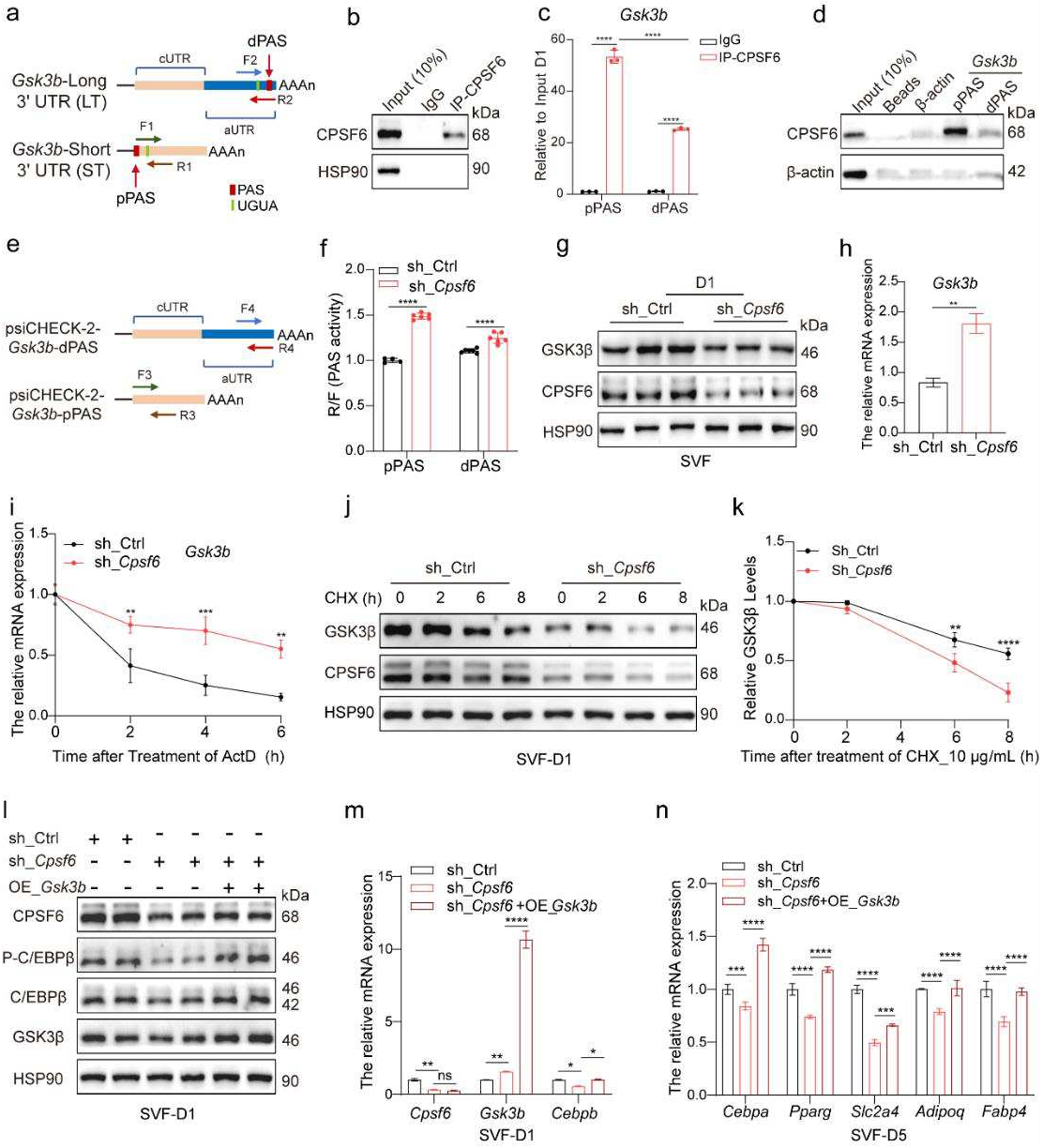


Fig. 5. CPSF6-mediated alternative polyadenylation regulates GSK3β expression during adipogenesis.

(a) Schematic representation of *Gsk3b* long (LT) and short (ST) transcripts generated by distal (dPAS) and proximal (pPAS) poly(A) site usage, respectively. **(b)** Immunoblot validation of CPSF6 RNA immunoprecipitation (RIP) in SVF cells at D1 of adipocyte differentiation. Input and IgG immunoprecipitation samples were included as controls. **(c)** RT-qPCR analysis of the enrichment of the *Gsk3b* dPAS- and pPAS-containing regions in CPSF6 RIP samples relative to IgG controls. **(d)** RNA pull-down assay showing the association of CPSF6 with the pPAS- and dPAS-containing regions of the *Gsk3b* 3'UTR. A *β-actin* coding-sequence fragment served as a negative control, and 10% of the SVF-D1 lysate was used as input. **(e)** Schematic representation of the dual-luciferase reporter constructs containing the *Gsk3b* pPAS- and dPAS-containing 3'UTR regions. **(f)** Dual-luciferase reporter assay measuring the effects of the *Gsk3b* pPAS- and dPAS-containing 3'UTR regions in SVF cells transduced with a *Cpsf6*-knockdown lentivirus and subsequently transiently transfected with the indicated reporter constructs. (*n* = 6). **(g-h)** Immunoblot **(g)** and RT-qPCR **(h)** analyses of GSK3β protein and *Gsk3b* mRNA

levels, respectively, in control and *Cpsf6*-knockdown SVF cells at D1 of adipocyte differentiation. GSK3β protein abundance was normalized to HSP90, and *Gsk3b* mRNA expression was normalized to *18S* rRNA. (n = 3). **(i)** RT-qPCR analysis of *Gsk3b* mRNA stability in control and *Cpsf6*-knockdown SVF cells after actinomycin D (ActD) treatment. Total RNA was collected at the indicated points. (n = 3). **(j-k)** Cycloheximide (CHX, 10 μg/mL) chase analysis of GSK3β protein stability in control and *Cpsf6*-knockdown SVF cells. Cell lysates were immunoblotted against GSK3β **(j)**, with degradation kinetics quantified in **(k)**. **(l)** Immunoblot analysis of phospho-C/EBPβ, total C/EBPβ, GSK3β, and CPSF6 in control and *Cpsf6*-knockdown SVF cells with or without *Gsk3b* overexpression at D1 of adipocyte differentiation. HSP90 served as a loading control. **(m)** RT-qPCR analysis of the indicated transcripts in the corresponding cells. (n = 3). **(n)** RT-qPCR analysis of adipogenic/mature adipocyte marker gene expression in control and *Cpsf6*-knockdown SVF cells with or without *Gsk3b* overexpression at D5 of adipocyte differentiation. (n = 3). Data are presented as mean ± SEM. Statistical analyses were performed using two-tailed unpaired Student's t-test, or two-way ANOVA followed by Sidak's multiple-comparisons test, as appropriate. n values are indicated in the corresponding panels. $^{*}P < 0.05$, $^{**}P < 0.01$, $^{***}P < 0.001$, $^{****}P < 0.0001$.

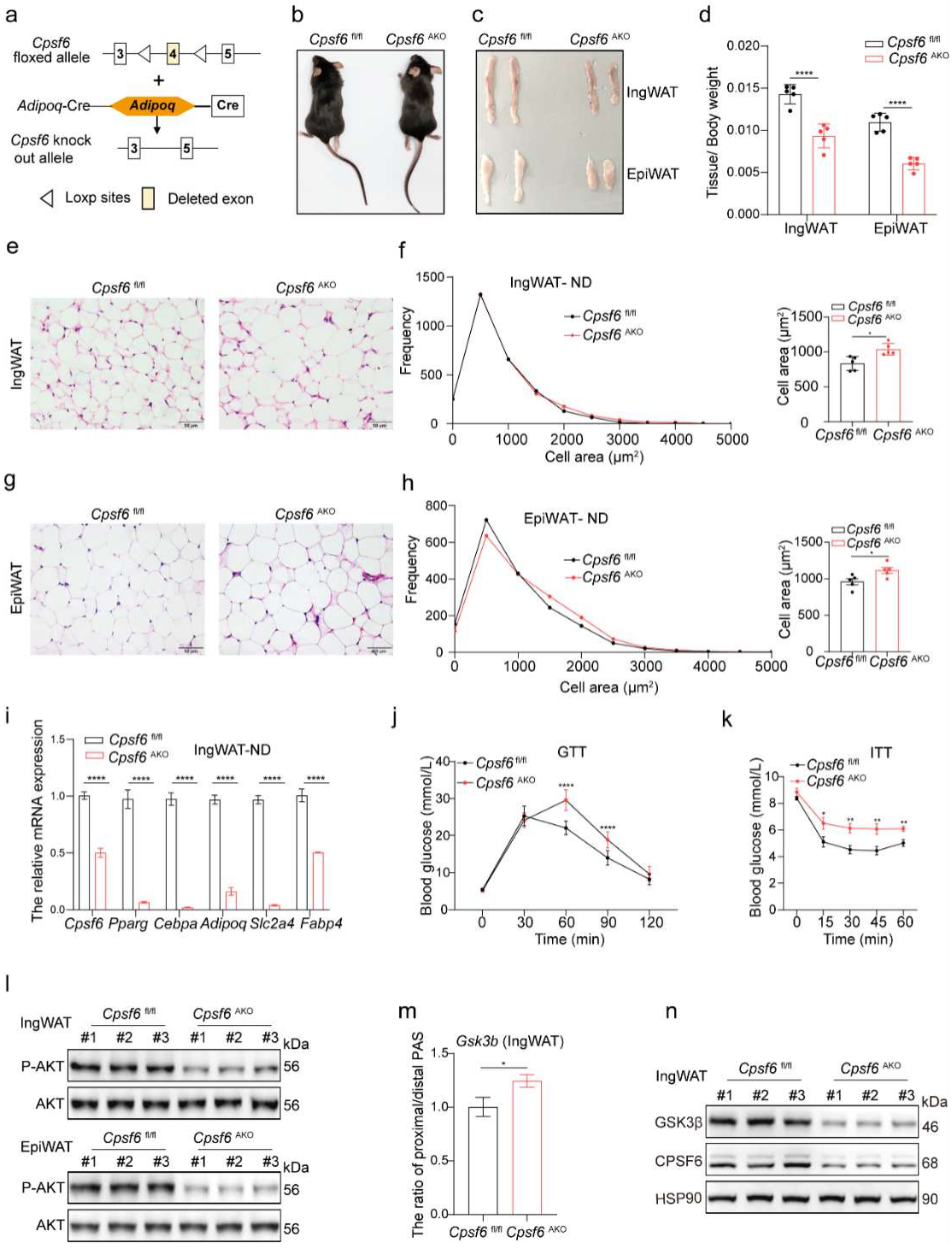


Fig. 6. Adipocyte-specific loss of *Cpsf6* disrupts white adipose tissue homeostasis and insulin sensitivity through aberrant APA regulation of *Gsk3b*.

(a) Schematic of the strategy used to generate adipocyte-specific *Cpsf6* knockout (*Cpsf6*^{AKO}) mice using the *adipoq*-Cre/loxP system. *Cpsf6*$^{fl/fl}$ (floxed *Cpsf6*) mice were crossed with *adipoq*-Cre transgenic mice to selectively delete *Cpsf6* in mature adipocytes. *Cpsf6*$^{fl/fl}$ littermates served as controls. **(b)** Representative gross appearance of *Cpsf6*$^{fl/fl}$ control and *Cpsf6*^{AKO} mice at 8 weeks of age maintained on a normal chow diet. **(c)** Representative images of IngWAT and EpiWAT depots isolated from *Cpsf6*$^{fl/fl}$ control and *Cpsf6*^{AKO} mice. **(d)** Relative weights of IngWAT and EpiWAT normalized to body weight in *Cpsf6*$^{fl/fl}$ control and *Cpsf6*^{AKO}

mice. (n = 5). **(e)** Representative H&E-stained sections of IngWAT from *Cpsf6*$^{fl/fl}$ control and *Cpsf6*^{AKO} mice. (Scale bar = 50 μm; n = 5). **(f)** Quantification of adipocyte size distribution (left) and mean adipocyte area (right) in IngWAT from *Cpsf6*$^{fl/fl}$ control and *Cpsf6*^{AKO} mice. **(g)** Representative H&E-stained sections of EpiWAT from *Cpsf6*$^{fl/fl}$ control and *Cpsf6*^{AKO} mice. (Scale bar = 50 μm; n = 5). **(h)** Quantification of adipocyte size distribution (left) and mean adipocyte area (right) in EpiWAT from *Cpsf6*$^{fl/fl}$ control and *Cpsf6*^{AKO} mice**. (i)** RT-qPCR analysis of mRNA expression of adipogenic and mature adipocyte marker genes (*Pparg*, *Cebpa*, *Adipoq*, *Fabp4*, and *Slc2a4*) in IngWAT from *Cpsf6*$^{fl/fl}$ control and *Cpsf6*^{AKO} mice. **(j)** GTT in *Cpsf6*$^{fl/fl}$ control and *Cpsf6*^{AKO} mice. Blood glucose levels were measured at the indicated time points after intraperitoneal glucose injection. **(k)** ITT in *Cpsf6*$^{fl/fl}$ and *Cpsf6*^{AKO} mice. Blood glucose concentrations were measured after intraperitoneal insulin injection. **(l)** Immunoblot analysis of insulin-stimulated AKT phosphorylation at Ser473 in IngWAT and EpiWAT from *Cpsf6*$^{fl/fl}$ control and *Cpsf6*^{AKO} mice. Total AKT was used as a loading control. **(m)** RT-qPCR analysis of proximal and distal poly(A) site usage of *Gsk3b* transcripts in IngWAT *Cpsf6*$^{fl/fl}$ control and *Cpsf6*^{AKO} mice. **(n)** Immunoblot analysis of CPSF6 and GSK3β protein expression in IngWAT from *Cpsf6*$^{fl/fl}$ and *Cpsf6*^{AKO} mice. Data are presented as the mean ± SEM. Statistical analyses were performed using two-tailed unpaired Student's t-test, one-way ANOVA, or two-way ANOVA, as appropriate, followed by Sidak's multiple-comparisons test. n values are indicated in the corresponding panels. $^{*}P < 0.05$, $^{**}P < 0.01$, $^{****}P < 0.0001$.

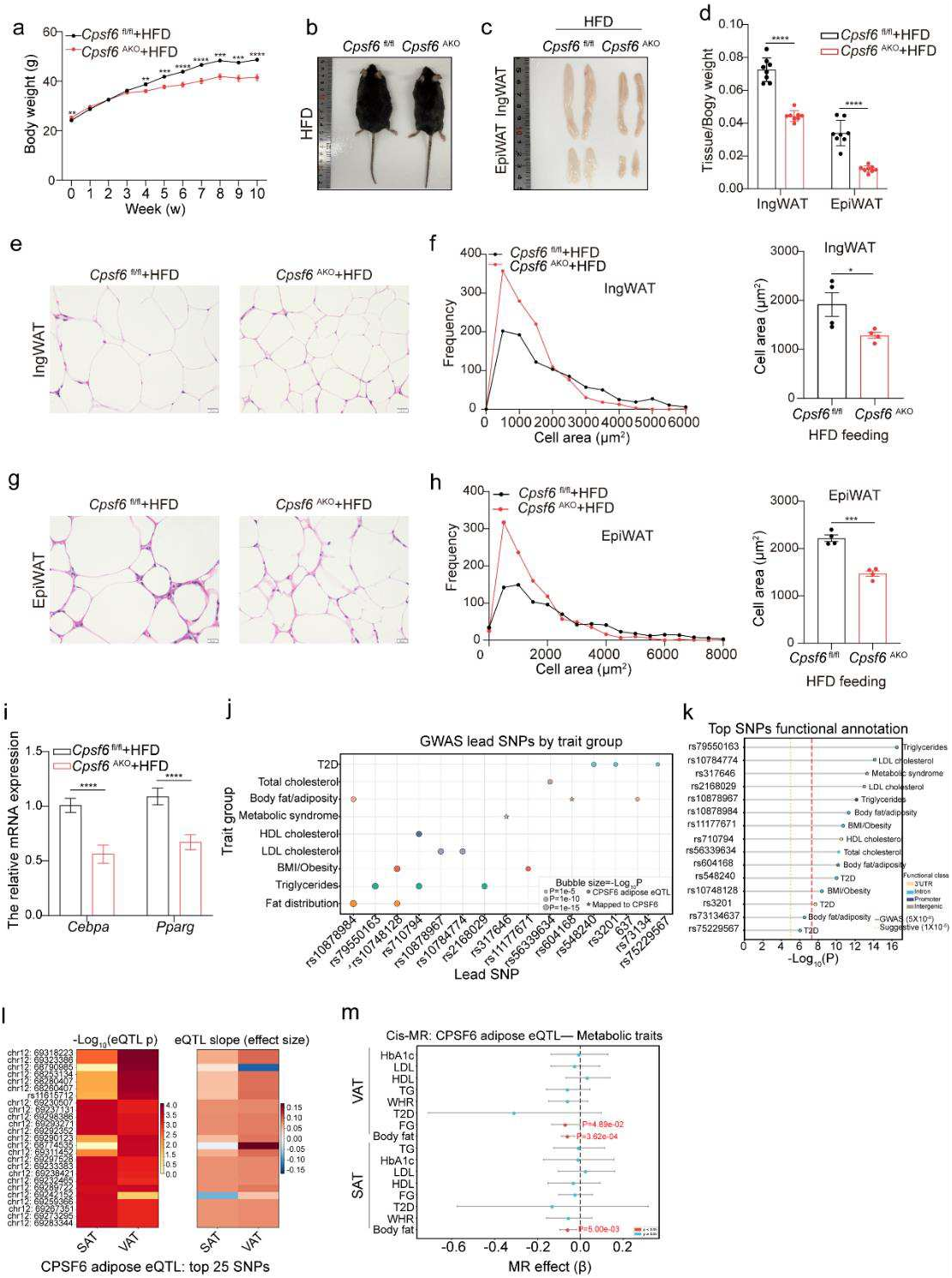
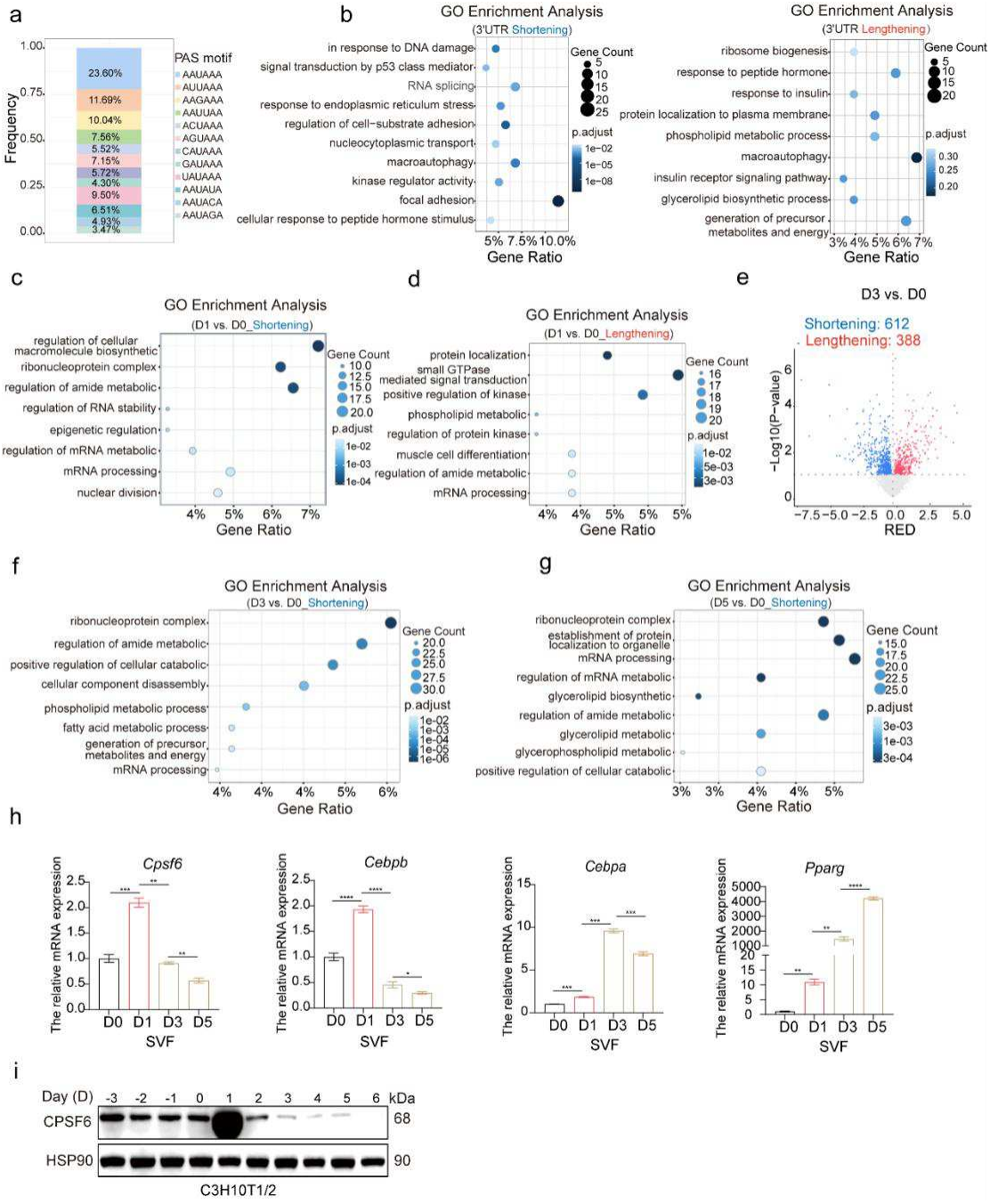


Fig. 7. Adipocyte-specific *Cpsf6* deletion disrupts adipose tissue remodeling during diet-induced obesity, and human genetic analyses link *CPSF6* to metabolic traits.

(a) Body weight curves of *Cpsf6*$^{fl/fl}$ control and *Cpsf6*^{AKO} mice during high-fat diet (HFD) feeding. **(b)** Representative gross appearance of *Cpsf6*$^{fl/fl}$ control and *Cpsf6*^{AKO} mice after HFD feeding. **(c)** Representative images of IngWAT and EpiWAT isolated from HFD-fed *Cpsf6*$^{fl/fl}$ control and *Cpsf6*^{AKO} mice. **(d)** Relative weights of IngWAT and EpiWAT, normalized to body weight, in HFD-fed *Cpsf6*$^{fl/fl}$ control and *Cpsf6*^{AKO} mice. (n = 8). **(e)** Representative H&E-stained sections of IngWAT from HFD-fed *Cpsf6*$^{fl/fl}$ control and *Cpsf6*^{AKO} mice. (Scale bar =

20 μm; $n = 4$). **(f)** Adipocyte area distribution (left) and mean adipocyte area (right) in IngWAT from HFD-fed *Cpsf6*$^{fl/fl}$ control and *Cpsf6*^{AKO} mice. **(g)** Representative H&E-stained sections of EpiWAT from HFD-fed *Cpsf6*$^{fl/fl}$ control and *Cpsf6*^{AKO} mice. (Scale bar = 20 μm; $n = 4$). **(h)** Adipocyte area distribution (left) and mean adipocyte area (right) in EpiWAT from HFD-fed *Cpsf6*$^{fl/fl}$ control and *Cpsf6*^{AKO} mice. **(i)** RT-qPCR of *Cebpa* and *Pparg* in IngWAT from HFD-fed *Cpsf6*$^{fl/fl}$ control and *Cpsf6*^{AKO} mice. Relative mRNA levels were normalized to *18S* rRNA. **(j)** Bubble plot summarizing metabolic trait-associated lead single-nucleotide polymorphisms (SNPs) identified in genome-wide association studies (GWAS) within the chr12q15 region surrounding *CPSF6*. Variants are grouped according to metabolic trait category and reported trait. Bubble size represents association significance ($-\log_{10}$P), and star symbols indicate variants mapped to *CPSF6* in the GWAS Catalog. **(k)** Predicted functional annotation of prioritized lead SNPs in the *CPSF6* region. Colors indicate functional categories, including 3'UTR, intronic, promoter, and intergenic variants; associated metabolic traits are indicated. The x axis shows GWAS association significance ($-\log_{10}$P). Stars are as defined in **(j)**. Dashed lines indicate genome-wide ($P = 5\times10^{-8}$) and suggestive ($P = 1\times10^{-5}$) significance thresholds. **(l)** Heatmaps showing the overlap between metabolic trait-associated GWAS variants in the chr12q15 region surrounding *CPSF6* and adipose tissue cis-expression quantitative trait locus (cis-eQTL) signals for *CPSF6* from the Genotype-Tissue Expression (GTEx) project. Rows indicate overlapping GWAS variants, and columns indicate human subcutaneous adipose tissue and visceral omental adipose tissue (VAT). The left heatmap shows eQTL association significance ($-\log_{10}$P), and the right heatmap shows eQTL effect sizes (slope). Positive and negative slopes indicate associations of the effect allele with increased and decreased *CPSF6* expression, respectively. **(m)** Single-variant cis-Mendelian randomization (cis-MR) analysis evaluating associations between genetically predicted *CPSF6* expression in human SAT or VAT and metabolic traits. The top cis-eQTL for *CPSF6* in each adipose depot was used as the instrumental variable, and effect estimates were calculated using the Wald-ratio method. Data are presented as the mean ± SEM. Statistical analyses were performed using two-tailed unpaired Student's t-test, or two-way ANOVA, as appropriate, followed by Sidak's multiple-comparisons test. *n* values are indicated in the corresponding panels. $^{*}P < 0.05$, $^{**}P < 0.01$, $^{***}P < 0.001$, $^{****}P < 0.0001$.

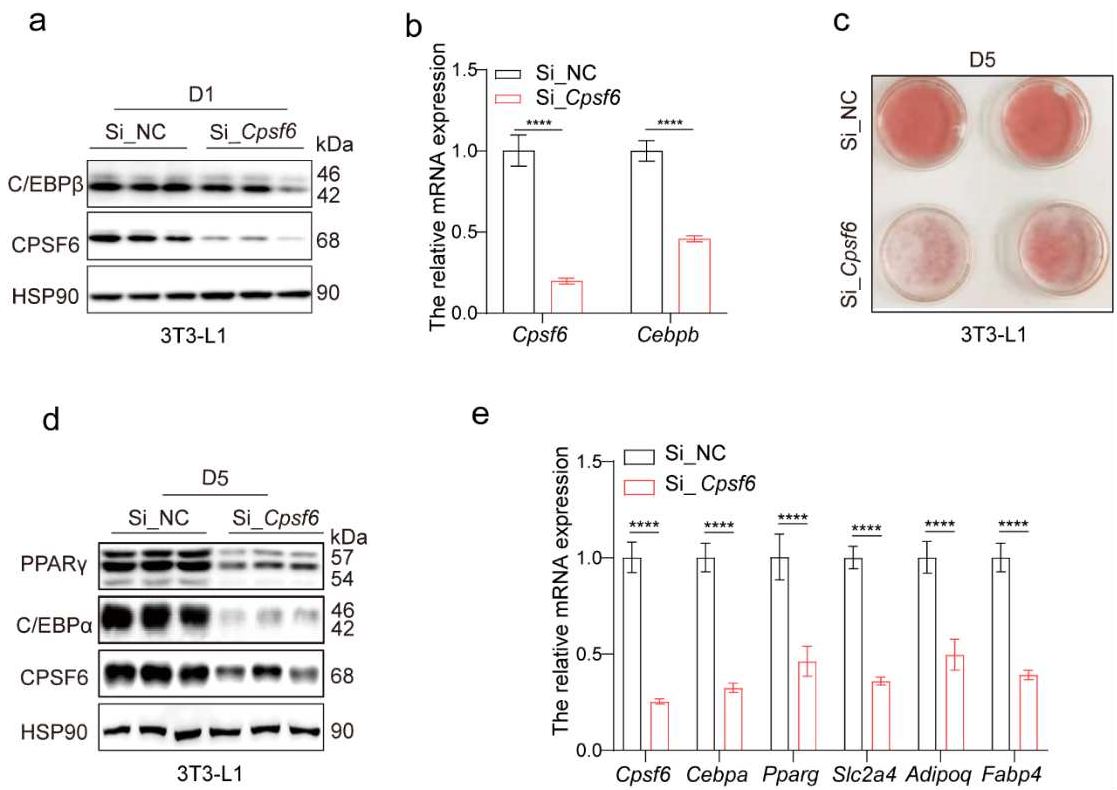
Extended Data Figures



Extended Data Fig. 1. Global APA features in obesity and during adipogenesis are accompanied by early induction of CPSF6.

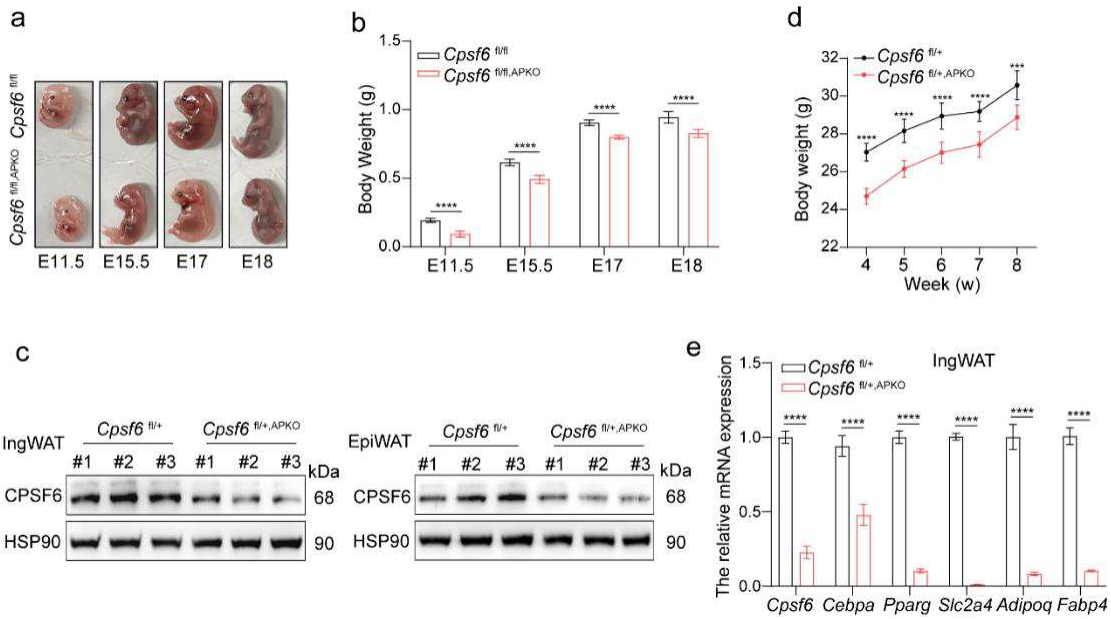
(a) Stacked bar plot displaying the relative usage frequencies of the canonical polyadenylation signal (PAS) motif (AAUAAA) and its 11 major variants, identified from global APA events in RNA-seq datasets from lean and obese adipose tissues. **(b)** Dot plots displaying Gene Ontology (GO) enrichment analysis of genes exhibiting significant 3'UTR shortening (left) and lengthening (right). These genes correspond to the global differential APA events identified from the same lean and obese adipose tissue transcriptomic datasets. Dot size denotes gene count, and the color gradient represents statistical significance (p.adjust). **(c-d)** GO enrichment analysis of genes exhibiting significant 3'UTR shortening **(c)** and lengthening **(d)** events at D1

versus (vs.) D0 during the adipocyte differentiation of primary SVF cells. **(e)** Volcano plot depicting the global dynamics of APA at D3 vs. D0. The x-axis represents the Relative Expression Difference (RED) between distal and proximal PAS isoforms (negative values: 3'UTR shortening; positive values: 3'UTR lengthening). The y-axis indicates -Log10(P-value), with the horizontal dotted line marking the significance threshold. Shortening and lengthening events are highlighted in blue and red, respectively. **(f-g)** GO enrichment analysis of genes exhibiting significant 3'UTR shortening events at D3 vs. D0 **(f)** and D5 vs. D0 **(g)**. **(h)** Bar graphs displaying the relative mRNA expression levels of *Cpsf6* and key adipogenic transcription factors (*Cebpb*, *Cebpa*, *Pparg*) during a 5-day adipocyte differentiation of SVF cells (D0, D1, D3, D5). **(i)** Immunoblot analysis showing the protein abundance of CPSF6 in C3H10T1/2 cells from day -3 to day 6 during adipogenic induction. HSP90 was used as an internal loading control. Molecular weights (kDa) are indicated on the right. Data are presented as mean ± SEM; $n = 3$. Statistical significance was determined by unpaired two-tailed Student's *t* test or one-way ANOVA with appropriate post hoc multiple-comparison testing. $^{**}P < 0.01$, $^{***}P < 0.001$, $^{****}P < 0.0001$.



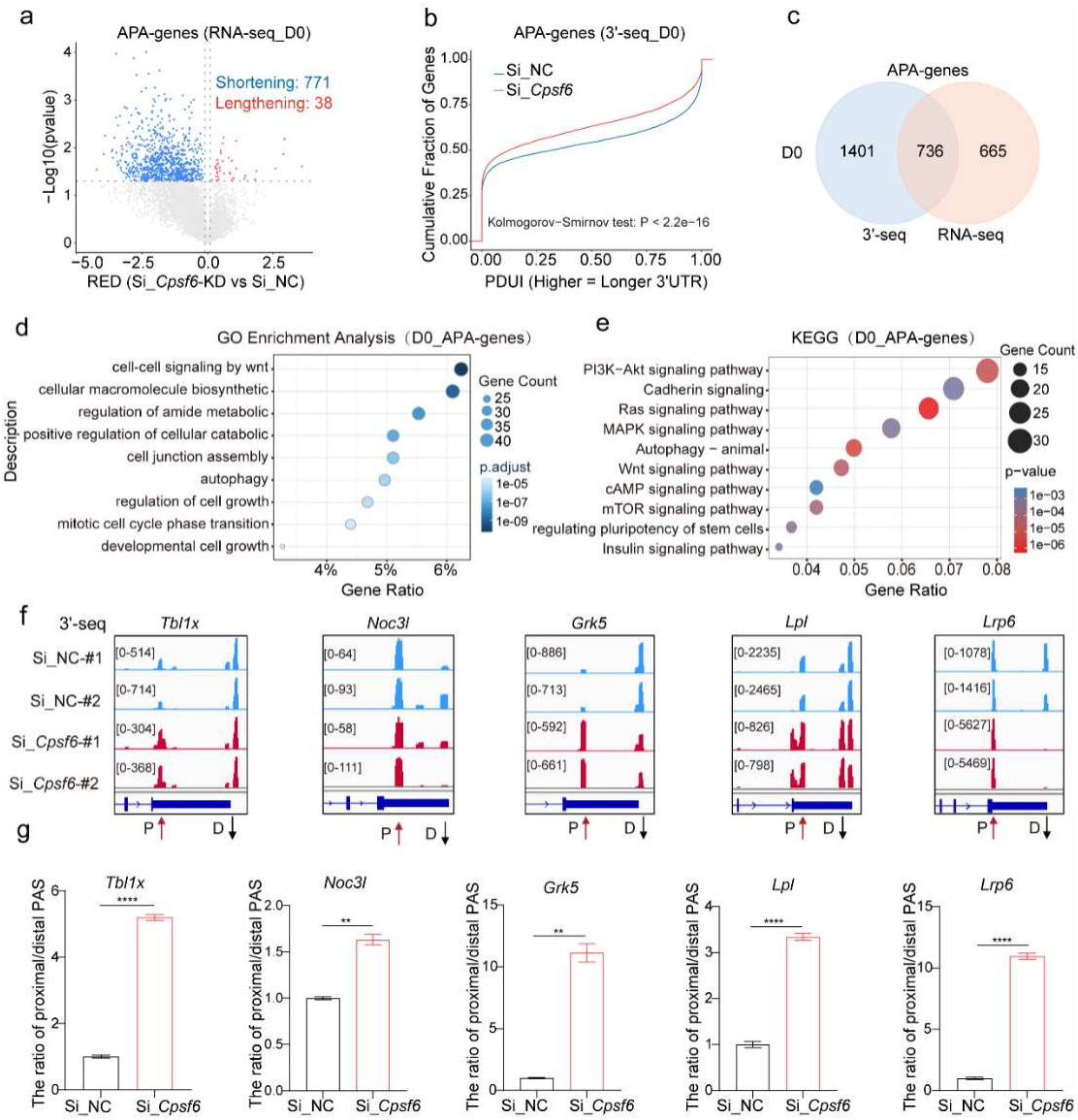
Extended Data Fig. 2. *Cpsf6* knockdown impairs adipocyte differentiation of 3T3-L1 preadipocytes.

(a-b) Immunoblot analysis of C/EBPβ and CPSF6 protein levels **(a)** and RT-qPCR analysis of *Cebpb* and *Cpsf6* mRNA levels **(b)** in 3T3-L1 cells transfected with control or *Cpsf6*-targeting siRNA on D1 of adipocyte differentiation. HSP90 and *18S* rRNA were used as loading and reference controls for immunoblotting and RT-qPCR, respectively. **(c)** Representative images of Oil-Red O staining in control and *Cpsf6*-knockdown 3T3-L1 cells on D5 of adipocyte differentiation. **(d)** Immunoblot analysis of PPARγ, C/EBPα, and CPSF6 protein levels in control and *Cpsf6*-knockdown 3T3-L1 cells on D5 of adipocyte differentiation. HSP90 was used as a loading control. **(e)** RT-qPCR analysis of *Cpsf6* knockdown efficiency and the expression of key adipogenic transcription factors (*Cebpa* and *Pparg*) and terminal differentiation markers (*Slc2a4*, *Adipoq*, and *Fabp4*) in control and *Cpsf6*-knockdown 3T3-L1 cells at D5 of adipocyte differentiation. *18S* rRNA was used as an internal control. Data are mean ± SEM; $n = 3$. $^{****}P < 0.0001$, two-way ANOVA with Sidak's multiple-comparisons test. si-*Cpsf6* denotes *Cpsf6*-targeting siRNA.



Extended Data Fig. 3. *Pdgfra*-Cre–mediated *Cpsf6* deletion causes embryonic growth restriction and reduces adipocyte marker gene expression in white adipose tissue.

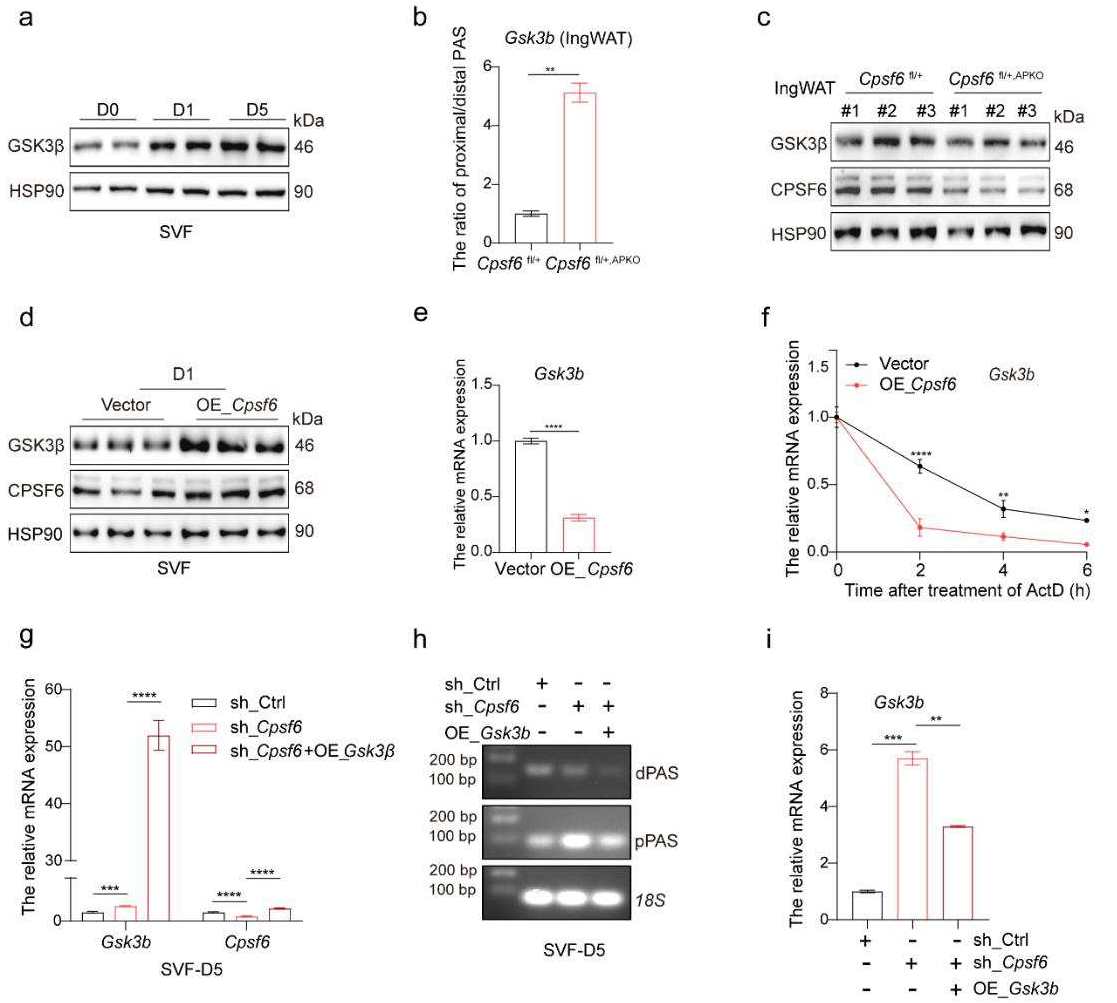
(a) Representative images of control and *Cpsf6*$^{fl/fl,\ Pdgfra\text{-}Cre}$ (*Cpsf6*^{APKO}) embryos at embryonic day (E) 11.5, E15.5, E17, and E18. *Cpsf6*^{APKO} embryos exhibited reduced body size compared with *Cpsf6*$^{fl/fl}$ control littermates. **(b)** Embryonic body weight of *Cpsf6*$^{fl/fl}$ control and *Cpsf6*^{APKO} embryos at E11.5, E15.5, E17, and E18. **(c)** Immunoblot analysis of CPSF6 in inguinal white adipose tissue (IngWAT) and epididymal white adipose tissue (EpiWAT) from 8-week-old male *Cpsf6*$^{fl/+}$ control and *Cpsf6*$^{fl/+,\ APKO\ mice}$. HSP90 was used as a loading control. (n = 3). **(d)** Longitudinal body-weight measurements of male *Cpsf6*$^{fl/+}$ control and *Cpsf6*$^{fl/+,\ APKO\ mice}$ from 4 to 8 weeks of age. (n = 5). **(e)** RT-qPCR analysis of *Cpsf6* and adipogenic/mature adipocyte marker gene expression, including *Cebpa*, *Pparg*, *Slc2a4*, *Adipoq*, and *Fabp4*, in IngWAT from 8-week-old male *Cpsf6*$^{fl/+}$ control and *Cpsf6*$^{fl/+,\ APKO}$ mice. *18S* rRNA was used as an internal control. (n = 3). Data are presented as mean ± SEM. Statistical significance was determined by two-way ANOVA with Sidak's multiple-comparisons test. n values are indicated in the corresponding panels. $^{***}P < 0.001$, $^{****}P < 0.0001$.



Extended Data Fig. 4. CPSF6 depletion induces widespread APA remodeling during early adipogenesis.

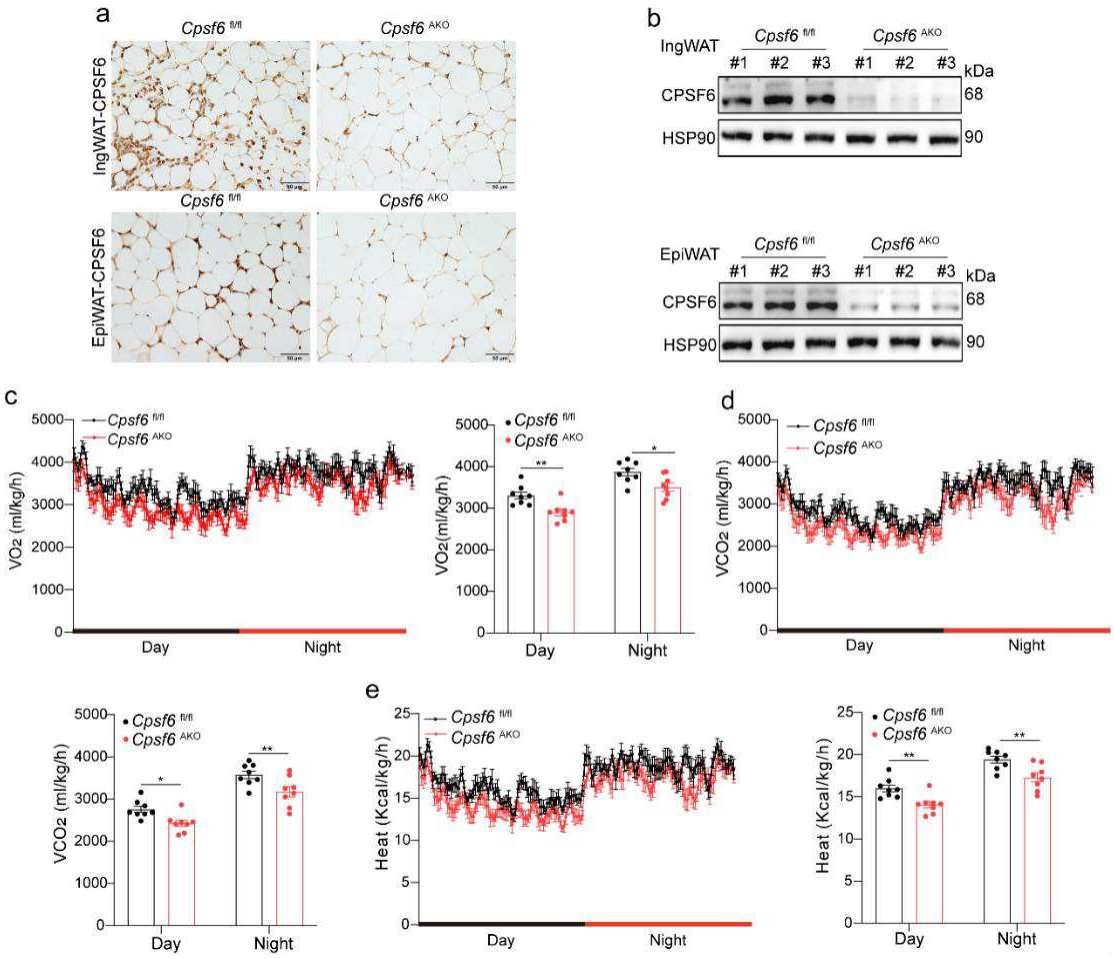
(a) Volcano plot showing differential APA events between control and si_*Cpsf6* cells at D0, identified by APAlyzer analysis of bulk RNA-seq data. Events showing significant 3'UTR shortening and lengthening are highlighted in blue and red, respectively. **(b)** Cumulative distribution of percentage distal poly(A) site usage index (*PDUI*) values in si_NC control and si_*Cpsf6* cells at D0, determined by 3'-seq. Statistical significance was assessed by the Kolmogorov-Smirnov test (all $P < 2.2 \times 10^{-16}$). **(c)** Venn diagram showing the overlap of differential APA genes identified by bulk RNA-seq and 3'-seq at D0. The corresponding gene list is provided in Supplementary Table S3. **(d-e)** Gene Ontology (GO) biological process enrichment **(d)** and Kyoto Encyclopedia of Genes and Genomes (KEGG) pathway enrichment **(e)** analyses of differential APA events identified by both bulk RNA-seq and 3'-seq at D0. **(f)** Representative IGV tracks showing 3'-seq read coverage at five additional APA-regulated genes in control and si_*Cpsf6* cells at D1. These genes were selected from the 12 APA genes shared by the two sequencing approaches within the adipogenesis-related gene set; the six genes with the largest Δ_*PDUI* values are presented in Figure 4. Red and black arrows indicate proximal (P) and distal (D) polyadenylation sites, respectively. **(g)** RT-qPCR validation of

APA-associated isoform changes for the five additional genes shown in **(f).** Primer sequences are provided in Supplementary Table S1. Expression levels were normalized to the mean value of the control group. Data are presented as mean ± SEM; $n = 3$. P values were determined using two-sided unpaired Student's *t*-tests.



Extended Data Fig. 5. CPSF6-dependent alternative polyadenylation modulates GSK3β expression in adipose tissue and during adipogenesis.

(a) Immunoblot analysis of GSK3β protein abundance in SVF cells at D0, D1, and D5 of adipocyte differentiation. **(b)** RT-qPCR analysis of pPAS- and dPAS-associated *Gsk3b* isoform usage in IngWAT from *Cpsf6*$^{fl/+}$ control and *Cpsf6*$^{fl/+,\ APKO}$ mice. **(c)** Immunoblot analysis of CPSF6 and GSK3β protein expression in IngWAT from *Cpsf6*$^{fl/+}$ control and *Cpsf6*$^{fl/+,\ APKO}$ mice. **(d-e)** Immunoblot **(d)** and RT-qPCR **(e)** analyses of GSK3β protein and *Gsk3b* mRNA levels, respectively, in control and *Cpsf6*-overexpressing SVF cells at D1 of adipocyte differentiation. GSK3β protein abundance was normalized to HSP90, and *Gsk3b* mRNA expression was normalized to *18S* rRNA. **(f)** RT-qPCR analysis of *Gsk3b* mRNA stability in control and *Cpsf6*-overexpressing SVF cells at D1 of adipocyte differentiation following treatment with actinomycin D (ActD) for the indicated times. **(g)** RT-qPCR analysis of *Gsk3b* and *Cpsf6* mRNA expression in control and *Cpsf6*-knockdown SVF cells with or without *Gsk3b* overexpression at D5 of adipocyte differentiation. **(h-i)** PCR **(h)** and RT-qPCR **(i)** analyses of *Gsk3b* APA isoform usage in control and *Cpsf6*-knockdown SVF cells with or without *Gsk3b* overexpression at D5 of adipocyte differentiation. Primer sequences are provided in Supplementary Table S1. Data are presented as mean ± SEM; $n = 3$. Statistical analyses were performed using two-tailed unpaired Student's t-test, one-way ANOVA, or two-way ANOVA, as appropriate, followed by Sidak's multiple-comparisons test. $^{*}P < 0.05$, $^{**}P < 0.01$, $^{***}P < 0.001$, $^{****}P < 0.0001$.



Extended Data Fig. 6. Characterization of adipocyte-specific *Cpsf6* knockout mice reveals altered whole-body energy metabolism.

(a-b) Validation of CPSF6 protein loss in IngWAT and EpiWAT from *Cpsf6*$^{fl/fl}$ control and adipocyte-specific *Cpsf6* knockout (*Cpsf6*^{AKO}) mice by immunohistochemistry **(a)** and immunoblotting **(b)**. Top, IngWAT; bottom, EpiWAT. HSP90 served as a loading control. **(c-e)** Indirect calorimetry analysis of oxygen consumption **(**VO_2; **c)**, carbon dioxide production **(**VCO_2; **d)**, and heat production **(e)** in *Cpsf6*$^{fl/fl}$ control and *Cpsf6*^{AKO} mice during the light and dark phases. ($n = 8$). Data are presented as mean ± SEM. Statistical significance was determined by two-way ANOVA followed by Sidak's multiple-comparisons test. *n* values are indicated in the corresponding panels. $^{*}P < 0.05$, $^{**}P < 0.01$, $^{****}P < 0.0001$.

Supplementary Files

This is a list of supplementary files associated with this preprint. Click to download.

- Graphicalabstract.pdf
- SupplementaryTables.pdf
- 20261026RAWGelsBlotsimages.pdf